Effective Mechanical Properties of 3D Structural Metamaterials

Mohamed Abdelhamid

A THESIS SUBMITTED TO

THE FACULTY OF GRADUATE STUDIES

IN PARTIAL FULFILLMENT OF THE REQUIREMENTS

FOR THE DEGREE OF

MASTER OF APPLIED SCIENCE

GRADUATE PROGRAM IN MECHANICAL ENGINEERING

YORK UNIVERSITY

TORONTO, ONTARIO

August 2017

Abstract

Recent advances in fabrication techniques have enabled the creation of novel materials with enhanced mechanical properties commonly known as metamaterials. They refer to materials consisting of a unit cell tessellated in three orthogonal directions with dimensions scaling down to the nanoscale. The objective of this research was to describe the effective properties of the octet-truss unit cell at different lattice angles and loading directions. The research is composed of three consecutive parts. The first part addressed the analytical derivation of the continuum-based model while including the lattice angle. The second part demonstrated the impact of the lattice angle on its effective properties, namely relative density, effective stiffness, and effective strength. Finally, potential in lattice structure optimization is demonstrated through an experimental study. This work addressed optimizing the structural configuration of the octet-truss, which when combined with favorable size effects, would unlock the full potential of mechanical metamaterials as load-bearing structures.

Acknowledgements

I would like to extend my appreciation and gratitude to my supervisor Dr. Aleksander Czekanski for his continuous and unconditional support through the course of my studies. I would like also to thank my parents, wife, and son for their support and encouragement and for enduring the late nights and long hours. I am grateful for all my colleagues in IDEA-Lab, for their support and for making IDEA-Lab a fun place to be. Finally, thanks to all my Egyptian friends at YorkU, for making Canada feel like home.

Notations

θ	Lattice angle
$\bar{\rho}$	Relative density
E_{eff}	Macroscopic/effective elastic modulus
σ_{eff}	Macroscopic/effective strength
Z	Nodal connectivity
L	Base side length of the tetrahedron prism (section 3.1)
	Length of square rod (section 3.2)
A_c	Cross-sectional area of the tetrahedron truss members
Σ_{ij}	Effective stress
E_{ij}	Effective strain (section 3.1)
	Strain tensor of the bulk body (section 3.2)
$\sigma^{(k)}$	Local stress in member k
$\varepsilon^{(k)}$	Local strain in member k
$A^{(k)}$	Cross-sectional area of member k
$L^{(k)}$	Length of member k
$V_v^{(k)}$	Volume fraction of member k
$N_{ij}^{(k)}$	Linear operator describing the transformation from local to global coordinates of member k
n_i, n_j	Direction vector components of member k
$E_s^{(k)}$	Elastic modulus of the constituent material of member k
C_{ijkl}	Macroscopic stiffness tensor
S_{ijkl}	Macroscopic compliance tensor
R	Radius of circular solid rod
	Mean radius of circular hollow rod
P	Tensile force

d	Infinitesimal film thickness
σ_{ij}	Stress tensor of the bulk body
τ_{ij}	Stress tensor of the surface
ε_{ij}	Strain tensor of the surface
λ, μ	Lame's constants of the bulk body
λ_s, μ_s	Lame's constants of the surface
E_b	Elastic modulus of the bulk body
E_s	Elastic modulus of the surface
E_{zz}	Uniaxial bulk body strain in the z direction
ε_{zz}	Uniaxial surface strain in the z direction
$d\Omega$	Infinitesimal cross-sectional area of the bulk body
ds	Infinitesimal cross-sectional area of the surface
E_f	Effective elastic modulus of the homogenous rod
R_c	Critical radius of the homogenous rod
t	Thickness of circular hollow rod
t_c	Critical thickness of homogenous hollow rod
a	Width of square rod
r	Radius of individual tetrahedron member
E_{11}''	Effective elastic modulus in a general direction defined by x'' axis
S_{11}''	Effective compliance in a general direction defined by x'' axis
$\{\sigma_{xyz}\}$	Stress vector in x, y, z coordinate system
$\{\sigma'_{xyz}\}$	Stress vector in x', y', z' coordinate system
$\{\sigma''_{xyz}\}$	Stress vector in x'', y'', z'' coordinate system
$[T_1]$	First stress transformation matrix between x, y, z and x', y', z'
$[T_3]$	Second stress transformation matrix between x', y', z' and x'', y'', z''
$[T_2]$	First strain transformation matrix between x, y, z and x', y', z'
$[T_4]$	Second strain transformation matrix between x', y', z' and x'', y'', z''
$[S']$	Compliance tensor in x', y', z' coordinate system
$[S'']$	Compliance tensor in x'', y'', z'' coordinate system

α, ϕ	Angles defining the general loading direction along x'' axis
G	Effective shear modulus
ν	Effective Poisson's ratio
$\bar{\varepsilon}_{ij}$	Effective/macroscopic strain
$[\bar{\sigma}'']$	General stress tensor applied through a general direction along x'' axis
σ_{lim}	Limit stress of the constituent material of the tetrahedron members
$\bar{\sigma}_{max}$	Maximum effective lattice strength
$\bar{\sigma}_{zz}$	Effective compressive stress applied along the z axis
$\bar{\sigma}_{xz}$	Effective shear stress applied along the $x - z$ plane
$\bar{\sigma}_{xx}$	Effective compressive stress applied along the x axis
$\bar{\sigma}_{yy}$	Effective compressive stress applied along the y axis
σ_y	Yield strength of the constituent material of the tetrahedron members
$E_{lattice}$	Elastic modulus of the lattice structure

Table of Contents

List of Tables

List of Figures

Chapter 1 Introduction and Justification

Summary: In this chapter, we define the problem, justify the undertaking of the study and outline the method of approach adopted in achieving the intended objectives. Furthermore, we provide a summary of the layout of the thesis.

1.1. Structural Metamaterials

Architectural materials refer to materials consisting of a unit cell that is tessellated in three dimensions to form a lattice structure. With the advent of size effects in the form of different mechanical properties at dimensions on the micro and nano lengthscales, the new field of metamaterials came to light. To fully unlock the potential of mechanical metamaterials, size effects need to be combined with structural effects, which refer to optimally arranging the individual members in the best possible configuration to carry the loads.

Different types of lattice structures have been studied in the past for a wide range of applications such as space structures and sandwich panels. The octet-truss is one of the favorable unit cells due to its efficient stretching-dominated behavior. However, the previous research didn't fully describe its properties since the new application of mechanical metamaterials was not in mind.

1.2. Justification of the Study

A number of studies have been performed on the octet-truss lattice since late 1960s. Most of

the early research had either one of two main applications in mind; large space structures or sandwich panels. Two of the significant parameters impacting the effective properties of the octet-truss lattice are the lattice angle parameter and the loading direction. Both of which were almost totally neglected in previous studies of the octet-truss.

Current metamaterials research performed on the octet-truss focuses on traditional loading directions along the x, y, z axes and the case of cubic symmetry (i.e. lattice angle $\theta = 45°$). The optimal stiffness and strength values doesn't always align with these configurations, which hinders the full utilization of lattice structures as load bearing structures.

From this aspect, derivation of the analytical model of the octet-truss lattice while including the lattice angle parameter and describing its effective properties under different loading conditions are crucial steps towards fully unlocking its potential.

Metamaterials have potential for multi-functional applications, for instance having a certain mechanical property with a thermal or electrical property such as thermal or electrical conductivity. Hence, the same material can perform two applications, such as energy storage and mechanical load-carrying capacity [1]. In addition, metamaterials have the potential of creating whole new classes of materials with unprecedented properties, such as exceptional load-carrying capacity and tailored energy storage characteristics for mechanical metamaterials [2].

1.3. Research Objectives

This thesis is dedicated to studying the effective properties of the octet-truss lattice at different lattice angles and different loading directions. Specifically, our current efforts were

devoted to:

(i) Analytical derivation of the stiffness/compliance tensors of the octet-truss lattice while including the lattice angle parameter θ.

(ii) Mathematically-modeling the size effects of metamaterials in the stiffness/compliance tensors of the octet-truss.

(iii) Extending the relative density formula of the octet-truss to include the lattice angle parameter up to a higher-order approximation.

(iv) Describing the effective stiffness of the octet-truss lattice and illustrating its variation with the lattice angle and loading direction.

(v) Studying the effective strength of the octet-truss lattice under a general loading condition and demonstrating its spatial distribution using tridimensional representations and collapse surfaces.

(vi) Demonstrating the potential of utilizing the octet-truss's effective properties in lattice structure optimization via a comparison with commercial optimization software. This is a crucial step towards fully unlocking the potential of metamaterials.

1.4. Method of Approach

The first step towards the achievement of the above-mentioned objectives was to derive the continuum-based model of the octet-truss from scratch while taking into account the lattice

angle parameter. This was performed through employing symmetry conditions to deduce the number of elastic constants and applying homogenization to determine their values. Following this step, the analytical model was further used to study the effective properties of the octet-truss. Namely; (i) the relative density formula was analytically extended to account for the lattice angle parameter, and further modified using curve fitting to a higher-order approximation, (ii) the effective stiffness behavior was studied against the lattice angle through the utilization of stiffness tensor transformations and analytical formulas describing the maximum and minimum as well as the specific elastic moduli, and (ii) the effective strength formula for a general loading direction was developed analytically, and subsequently used to demonstrate its behavior through tridimensional representations and collapse surface plots. Finally, potential in lattice structure optimization is demonstrated through a comparison with a commercial FEA software and experimentally verified through 3D printing and mechanical testing.

1.5. Layout of Thesis

This thesis is divided into six chapters in total. Following this brief introduction, **Chapter 2** provides a critical and comprehensive review of the relevant work available in literature on the effective properties of the octet-truss lattice structure and identifies the knowledge gaps. **Chapter 3** presents the analytical derivation of the continuum-based model of the octet-truss while taking into account the lattice angle parameter. In addition, a mathematical representation of the size effects is developed to be included in the stiffness/compliance tensors. In **Chapter 4**, we describe the effective properties of the octet-truss lattice while building upon the previously derived continuum-based model. Namely, we discuss the

relative density, the effective stiffness, and the effective strength. In **Chapter 5**, we address the finite element considerations of the octet-truss lattice and demonstrate the potential of the octet-truss in lattice structure optimization through a comparison with a commercial software followed by experimental testing. Finally, in **Chapter 6**, we conclude the work performed, identify the original contributions, and outline suggestions for future work.

Chapter 2 Literature Review

Summary: This chapter is dedicated to reviewing the existing literature on the research topic. It's divided into four main sections: (i) "Architectural Materials" provides a brief introduction to the concept of architectural or cellular materials and their mechanical properties. (ii) "Metamaterials" offers an introduction into the new field of architectural materials at the nanoscale, the main observed size effects, and the common fabrication techniques. (iii) "Constitutive Modeling of the Octet-truss" presents the previous research efforts in developing continuum models of the unit cell of choice (octet-truss) and subsequent studies of its effective mechanical properties. (iv) "Finite Element Modeling of the Octet-truss" discusses the earlier attempts in numerically-simulating the mechanical properties of the octet-truss lattice. Throughout the chapter, potential literature gaps are identified to be addressed in subsequent chapters.

2.1. Architectural Materials

In the last few decades there has been a growing interest in lightweight load-bearing structures. Inspiration from nature can be found in natural cellular materials like wood, honeycomb, butterfly wings and foam-like structures such as trabecular bones and sponge [3]. Architectural materials refer to materials consisting of a unit cell that is tessellated in three orthogonal dimensions to form a lattice structure. They have been successfully used to create mechanically-efficient engineering structures such as the Eiffel Tower and the Garabit Viaduct [4,5]. This class of materials combines the benefits of low density as it only occupies

a fraction of the monolithic bulk solid, and strength by arranging its elements efficiently to carry the loads. Previous studies have shown that the macroscopic mechanical properties of cellular materials depend on three parameters: the constituent material properties, the deformation mechanism, and the relative density $\bar{\rho}$ (defined as the solid volume within the unit cell divided by the volume of the unit cell). Cellular-solids theory predicts scaling relationships between the macroscopic stiffness E_{eff} and strength σ_{eff} and the relative density, namely $E_{eff} \propto \bar{\rho}^{m}$ and $\sigma_{eff} \propto \bar{\rho}^{n}$ respectively, where the dimensionless parameters m and n depend on the unit cell geometry [6].

For a 3D structure to be rigid (i.e. not to collapse upon itself), a minimum nodal connectivity of $Z = 6$ is required. A connectivity of $Z = 12$ categorizes the structure as stretching-dominated where the lattice members deform by tension/compression. Bending-dominated structures that deform through the bending of their members has a connectivity of $6 \leq Z < 12$ [7,8]. For stretching-dominated structures such as the octet-truss lattice (Fig. 3. 1a), these scaling relationships are linear. On the other hand, for bending-dominated structures such as honeycombs and the octahedral lattice, these relationships are quadratic or higher [1,9].

2.2. Metamaterials

Some classes of materials, when their dimensions are scaled down below the micron length scale, start to exhibit different mechanical properties known as size effects. The type of materials that combine both structural and size effects are referred to as metamaterials. In the context of mechanical structures, metamaterials commonly refer to materials with certain mechanical properties defined by their geometry rather than their composition [3].

2.2.1. Size Effects

An example of these size-dependent changes is the observed strengthening in single crystalline metals. Compressive experiments performed by Greer and Nix (2005) on single crystalline gold pillars with diameters of $300 - 7450\ nm$ showed a strong size effect. The recorded yield stresses were much higher than the known yield stress of gold at 2% strain. In addition, the measured flow stresses were found to reach 4.5 GPa, a considerable fraction of the theoretical strength [10–14].

Another example is the observed transition from brittle to ductile behavior in metallic glasses and ceramics. Jang and Greer (2010) performed tension testing on zirconium-based metallic glass nanopillars fabricated using focused ion beam etching. The experiments showed that at a diameter of $100\ nm$, a yield strength of $2.25\ GPa$ typical of ceramic materials was achieved along with a fracture ductility of 25% typical of metallic alloys. This is unprecedented as high strength is usually achieved at the expense of low ductility [15,16].

A third example of size effects is smaller-is-weaker in nanocrystalline metals. Lian et al. (2011) performed compression experiments on thin-walled nanocrystalline Ni hollow cylinders of $500\ nm$ and $150\ nm$ thickness fabricated using electroless plating of vertical polymer cylinders. The testing results showed a sudden brittle collapse of the $500\ nm$ sample vs a gradual collapse of the $150\ nm$ at a much lower compressive strength than predicted analytically [17]. Further experiments were performed on nanocrystalline Pt nanopillars by Gu et al. (2012). They fabricated and compressively-tested nanocylinders with a grain size of $12\ nm$ and diameter-to-grain-size ratio between 5 and 80. The testing showed a sudden weakening in the compressive strength of samples below a certain ratio,

with the larger samples having a strength similar to the bulk material [18].

2.2.2. Manufacturing Techniques

Recent advances in additive manufacturing techniques have made it possible to manufacture lattice structures with more geometrical and dimensional freedom than ever. Metamaterials are usually fabricated as either hollow-tube or solid lattice structures. The former is preferable since the size effects are easier to exhibit in higher ratios of truss member free perimeter to solid cross-sectional area inherent in the hollow-tube case (see Section 3.2) [2]. Generally, fabrication of hollow-tube micro and nanolattices follows these steps: (i) A 3D CAD model is designed based on the internal geometry of the hollow-tube lattice. (ii) The model is fabricated in polymer using certain AM techniques like self-propagating photopolymer waveguides [19–23], projection micro stereolithography [3], or two-photon lithography [16,2,24–26]. (iii) A coating process is applied to deposit the desired material on the output polymer scaffold. This process could be sputtering deposition for metallic elements [2], atomic layer deposition for oxides, nitrides and metals [26,27], or electroless plating for nickel [3,22]. (iv) Using a milling technique (i.e. focused ion beam), the internal polymer scaffold is exposed by removing one or two sides of the newly deposited/coated material [12,25,28]. (v) Finally, the internal polymer scaffold is removed using thermal decomposition [3] or oxygen plasma etching [26–28].

2.3. Constitutive Modeling of the Octet-truss

Continuum constitutive models have been developed to describe the effective mechanical properties of the octet-truss lattice structure. A common assumption amongst these models

is that the lattice members are pin-jointed at all nodes, hence the contribution from the bending resistance of the members and nodes can be neglected compared to the axial tensile/compressive stiffness of the members [29]. Generally, symmetry considerations could be employed to deduce the number of independent constants in the macroscopic stiffness tensor. Following the pin-jointed assumption, these elastic constants are determined either by carefully-planned finite element simulations or by analytically averaging the contribution from each element to the macroscopic stiffness, which is achieved through 3D coordinate transformations [30,31].

Nayfeh and Hefzy (1978) derived a first order approximation of the relative density of the octet-truss lattice by dividing the solid volume within the unit cell by the total volume of the unit cell. They employed 3D coordinate transformation and volume averaging in order to obtain the macroscopic stiffness matrix* [30].

Lake (1992) constructed a strength tensor by converting applied stresses to strains for each parallel group of members using the macroscopic compliance matrix. Failure would occur in a member if its axial strain exceeded a critical value based on an elastic buckling limit. The choice of elastic buckling over plastic yielding is somehow justified given that space structures usually compose of slender members. Lake's strength tensor could easily accommodate multiaxial loading as well as different loading directions through coordinate

* Truss structures were considered in 1960s and 1970s as possible candidates for constructing large space structures, and most of the early researchers of the octet-truss had that specific application in mind. That is why most of the work published in that era was in space-related conferences and NASA technical publications.

transformation. The author also developed a 3D Cartesian plot of the uniaxial compression strength, from which he concluded the direction and value of the maximum strength of the octet-truss lattice for the case of cubic symmetry where the lattice angle θ equals 45° (θ is the angle between the individual truss members and the horizontal midplane as shown in Fig. 3. 1) [32].

Deshpande et al. (2001) investigated the effective properties of the octet-truss lattice structure both theoretically and experimentally. They validated the analytically-predicted elastic modulus and strength using FEM and experimental uniaxial compression of an octet-truss lattice made from a casting aluminum alloy. They also explored the collapse criteria of two competing mechanisms (plastic yielding and elastic Euler buckling) and plotted the collapse surfaces for these two mechanisms under different loading conditions. The macroscopic collapse stress was evaluated by equating the external work for the kinematically admissible modes of collapse: (i) to the plastic dissipation in stretching the struts for the case of plastic yielding, and (ii) to the internal work in buckling the struts for the case of elastic buckling. In addition, they proposed a third-order approximate formula for the relative density that includes a parameter dependent on the nodes' detailed geometry.

It is important to note that the previous studies were performed only for the case of cubic symmetry. At this angle, the octet-truss is considered to be at the highest possible level of symmetry. However, potential applications of metamaterials (e.g. thin-walled pressure vessels) necessitates the use of anisotropic lattice structures in order to achieve the optimal combination of low density and high direction-specific load-carrying capacity.

2.4. Finite Element Modeling of the Octet-truss

Deshpande et al. (2001) performed finite element simulations of the octet-truss lattice in order to assess the accuracy of their proposed analytical expressions of the elastic moduli. The octahedral substructure was selected to be modeled using 20-40 1D solid cylindrical beam elements to represent each truss member based on its length, while relaxing the pin-jointed nodes assumption. Boundary conditions were applied according to the symmetry considerations and also in order to prevent rigid body motion. In addition, they considered using three different values for the constituent material Poisson's ratio, which was found to have negligible effect on the resultant elastic moduli. Over a relative density range of 0.01 to 0.5, the authors found excellent agreement between their analytical predictions and the FEA results, which further supported the pin-jointed nodes assumption [8]. However, this work considered only the case of cubic symmetry with a lattice angle of $\theta = 45°$.

Wallach and Gibson (2001) numerically analyzed the octet-truss lattice under the pin-jointed nodes assumption using two methods: (i) a truss-analysis program in Matlab where they performed linear static analyses while modeling the truss members as linear springs, and (ii) a finite element model in Abaqus where they included nonlinear effects such as strain hardening and large deformations while modeling the truss members as truss elements. The FEM results were utilized to find the nine elastic constants comprising the compliance matrix. In addition, the authors also plotted the variation of the elastic constants (Young's moduli, shear moduli, and Poisson's ratios) as well as the uniaxial tensile and shear strengths vs the aspect ratio of the unit cell (an alternative parameter representing the lattice angle) [33]. However, the authors didn't take into account the effect of changing the truss member

geometry (e.g. diameter to length ratio) on the accuracy of the finite element predictions. In addition, the relative density formula used in calculating the specific elastic constants was a first-order approximation, hence not accurate for high-aspect-ratio, low-lattice-angle configurations.

Wallach and Gibson (2001a) also performed a defect sensitivity analysis to illustrate the effect of removing random truss members of the octet-truss lattice on the elastic constants. A linear relation was proven to exist between the modulus (and strength) and the fraction of members removed. By comparing their results to similar studies performed on open-cell foams, the authors demonstrated how the octet-truss lattice was more tolerant to defects than open-cell foams [34].

Hyun et al. (2003) utilized FEM to simulate the properties of Kagomé and octet-truss under shear and compression. It's worth noting that the researchers had the application of core sandwich panels in mind while deciding on the simulation parameters. Their simulation was performed for two different materials; Cu alloy with significant strain hardening and Al alloy with minor hardening. The unit cell and truss member geometry was selected to give a relative density of $\bar{\rho} \approx 0.02$, a near-optimized value for sandwich panels. This precludes the resultant conclusions from being reliably extended to different truss member geometries or lattice angles. The simulation employed 10-node tetrahedral solid elements and displacement control using large displacement theory to depict the softening upon reaching the buckling state. The researchers concluded the Kagomé core to have better compressive strength than the octet-truss. However, this was mainly because the optimum loading direction of the maximum compressive strength for the octet-truss wasn't simulated. They

also demonstrated the anisotropy of an octet-truss loaded in shear in contrast with the Kagomé, with the latter showing more isotropy with respect to shear loading [35].

Chapter 3 Constitutive Modeling of the Octet-truss Lattice

Summary: In order to understand how the octet-truss lattice structure behaves as a bulk (i.e. effective stress to strain relation), a continuum-based model is developed to relate the effective† stress-strain relation to the local stress-strain relation. Continuum-based models have been developed in previous work, however they only addressed the cubic symmetry case where the lattice angle $\theta = 45°$ (defined as the angle between the truss members and the horizontal midplane as in Fig. 3. 1) [8,32,36–39]. In the first section of this chapter, we intend to overcome this limitation by introducing the lattice angle parameter into the stiffness/compliance tensor. In the second section, the "Gurtin Murdoch" linearized theory of surface elasticity is utilized to mathematically model size effects. By including the resulting effective elastic modulus E_f in the stiffness and compliance tensors, they become fully representative of metamaterials at all lengthscales.

3.1. Continuum-based Modeling

In order to develop the model, we select the least substructure that composes the whole unit cell, which is a tetrahedron as shown in Fig. 3. 1a. The square prism enclosing the tetrahedron has two sides of length L and a height of length $L.tan(\theta)$, where the cubic

† Macroscopic, effective, or global are interchangeably used to refer to properties of the lattice structure as a continuum, as opposed to local or microscopic which refer to those of the individual truss members.

symmetry is achieved when the lattice angle $\theta = 45°$. The tetrahedron consists of six truss members of the same cross-sectional area A_c. Metamaterial structures are usually manufactured as hollow members of circular or elliptic cross section, this is mainly due to the manufacturing process which usually includes depositing a thin layer of metallic or ceramic alloy on a polymer scaffold, then etching the polymer away to produce a hollow-tube lattice structure. The elliptic cross section of the individual members is a characteristic of the two-photon lithography process (Nanoscribe GmbH) [40]. The hollow cross section of the individual members has a beneficial effect on the mechanical properties upon exploiting the size effects (see Section 3.2).

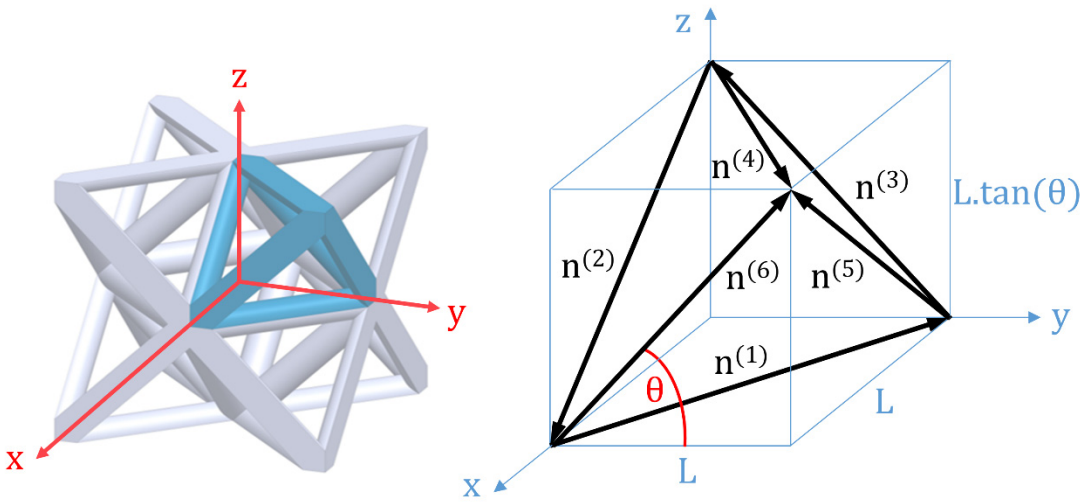

(a) (b)

Fig. 3. 1 Tetrahedron substructure: (a) The octet-truss unit cell with the tetrahedron substructure shown in blue, (b) The tetrahedron's six truss members.

Since the octet-truss unit cell is of the stretching-dominated type, the elastic stiffness of the lattice structure is directly related to the elastic uniaxial tensile/compressive stiffness of the individual truss members, while neglecting the bending resistance of the members and the

nodes. The assumption of pin-jointed nodes is valid in this case [39].

All tetrahedron truss members are transformed from their local coordinates to the global coordinates (x, y, z) as summarized in Table 3. 1. A homogenization process is applied to relate the microscopic properties of the individual truss members to the macroscopic properties of the lattice.

Truss Member		$n^{(1)}$	$n^{(2)}$	$n^{(3)}$	$n^{(4)}$	$n^{(5)}$	$n^{(6)}$
Unit Direction Vectors	e_1	$-1/\sqrt{2}$	$cos(\theta)$	0	$1/\sqrt{2}$	$cos(\theta)$	0
	e_2	$1/\sqrt{2}$	0	$cos(\theta)$	$1/\sqrt{2}$	0	$cos(\theta)$
	e_3	0	$-sin(\theta)$	$-sin(\theta)$	0	$sin(\theta)$	$sin(\theta)$
Length		$\sqrt{2}$L	$L/\cos(\theta)$	$L/\cos(\theta)$	$\sqrt{2}$L	$L/\cos(\theta)$	$L/\cos(\theta)$

Table 3. 1 Unit vector components and length of tetrahedron members.

Since the representative volume element in this case consists of discrete members, the averaging procedure is simplified greatly to become a summation instead of an integral (the reason behind using "continuum-based" term) [39]. The relation between the effective stress of the lattice structure and the local stress in the truss members is given by:

$$\Sigma_{ij} = \frac{1}{V}\sum_{m=1}^{m} \sigma^{(k)} N_{ij}^{(k)} A^{(k)} L^{(k)} = \sum_{m=1}^{m} V_v^{(k)} \sigma^{(k)} N_{ij}^{(k)} \tag{3.1}$$

where $k = 1, 2 \ldots 6$ refers to the truss member number and $i, j = 1, 2, 3$ refer to the direction vector components. The local to effective strain relation is given by:

$$\varepsilon^{(k)} = N_{ij}^{(k)} E_{ij} \tag{3.2}$$

where Σ_{ij}, E_{ij} are the effective stress and effective strain respectively. $\sigma^{(k)}, \varepsilon^{(k)}$ are the local stress and local strain in the k^{th} member respectively. $A^{(k)}, L^{(k)}$ are the cross-sectional area and length of the k^{th} member respectively. $V_v^{(k)}$ is the volume fraction of the k^{th} member (i.e. solid volume of member over total volume of tetrahedron). $N_{ij}^{(k)}$ is the linear operator describing the transformation from the local to global coordinates of the k^{th} member. This operator can be further simplified to the product of the truss member's direction vector components as follows [30]:

$$N_{ij}^{(k)} = n_i^{(k)} . n_j^{(k)} \tag{3.3}$$

Furthermore, the local stress-strain relation is given by:

$$\sigma^{(k)} = E_s^{(k)} \varepsilon^{(k)} \tag{3.4}$$

By substituting from Eq. 3.2 into Eq. 3.4, we get the local stress to global strain relation as follows:

$$\sigma^{(k)} = E_s^{(k)} N_{ij}^{(k)} E_{ij} \tag{3.5}$$

where $E_s^{(k)}$ is the elastic modulus of the k^{th} member, this value is constant for all members since the constituent material is assumed to be homogeneous and isotropic. By substituting from Eq. 3.5 in Eq. 3.1, we can determine the global stress-strain relation as follows:

$$\Sigma_{ij} = \sum_{m=1}^{m} V_v^{(k)} E_s^{(k)} N_{ij}^{(k)} N_{kl}^{(k)} E_{kl} \tag{3.6}$$

from which we can extract the macroscopic stiffness tensor components as follows:

$$C_{ijkl} = \sum_{m=1}^{m} V_v^{(k)} E_s^{(k)} N_{ij}^{(k)} N_{kl}^{(k)} = \sum_{m=1}^{m} V_v^{(k)} E_s^{(k)} n_i^{(k)} n_j^{(k)} n_k^{(k)} n_l^{(k)} \tag{3.7}$$

By substituting with values from Table 3. 1 in Eq. 3.7, we obtain the macroscopic stiffness tensor as follows:

$$C_{ijkl} = \frac{E_s A_c}{L^2} \times \begin{bmatrix} \frac{m + 2\sqrt{2}\, m^4}{2\sqrt{2}\, n} & \frac{m}{2\sqrt{2}\, n} & m^2 \cdot n & 0 & 0 & 0 \\ \frac{m}{2\sqrt{2}\, n} & \frac{m + 2\sqrt{2}\, m^4}{2\sqrt{2}\, n} & m^2 \cdot n & 0 & 0 & 0 \\ m^2 \cdot n & m^2 \cdot n & 2n^3 & 0 & 0 & 0 \\ 0 & 0 & 0 & m^2 \cdot n & 0 & 0 \\ 0 & 0 & 0 & 0 & m^2 \cdot n & 0 \\ 0 & 0 & 0 & 0 & 0 & \frac{m}{2\sqrt{2}\, n} \end{bmatrix} \tag{3.8}$$

The compliance tensor S is obtained by inverting the stiffness tensor as follows:

$$S_{ijkl} = \frac{L^2}{E_s A_c} \times \begin{bmatrix} \frac{n(\sqrt{2}\, m^3 + 1)}{2\, m^4} & \frac{n(\sqrt{2}\, m^3 - 1)}{2\, m^4} & \frac{-m}{\sqrt{2}\, n} & 0 & 0 & 0 \\ \frac{n(\sqrt{2}\, m^3 - 1)}{2\, m^4} & \frac{n(\sqrt{2}\, m^3 + 1)}{2\, m^4} & \frac{-m}{\sqrt{2}\, n} & 0 & 0 & 0 \\ \frac{-m}{\sqrt{2}\, n} & \frac{-m}{\sqrt{2}\, n} & \frac{\sqrt{2}\, m^3 + 1}{2\, n^3} & 0 & 0 & 0 \\ 0 & 0 & 0 & \frac{1}{m^2 \cdot n} & 0 & 0 \\ 0 & 0 & 0 & 0 & \frac{1}{m^2 \cdot n} & 0 \\ 0 & 0 & 0 & 0 & 0 & \frac{2\sqrt{2}\, n}{m} \end{bmatrix} \tag{3.9}$$

where $m = \cos(\theta)$ and $n = \sin(\theta)$.

It's worth noting that the stiffness of the octet-truss lattice depends on four main parameters: E_s the elastic modulus of the constituent material, A_c the cross-sectional area of the truss members, L the side length of the tetrahedron prism, and θ the lattice angle.

3.2. Modeling Size Effects in Metamaterials

The size effects observed as a change in the mechanical properties when the material dimensions reach the nanoscale can be modeled as surface effects. "Gurtin Murdoch" linearized-theory of surface elasticity can be used to mathematically model the elastic behavior of solids at the nanoscale [41]. In this theory, surface stress and surface energy can be modeled as a pre-stretched elastic thin film perfectly attached to the external surface of the bulk body. The difference between the classical theory of elasticity and this model is attributed to the traction boundary condition on the external surface of the bulk body [41]. This model can be interpreted physically as follows: the atoms at a free surface experience a different local environment than do atoms in the bulk body. Hence, the energy associated with surface atoms is, in general, different from that of atoms in the bulk body. This surface energy is typically neglected since the volume occupied by these surface atoms is negligible compared to the total bulk volume, however in nano-sized particles this value becomes significant [42].

Herein, this theory is applied to a simple case of 1D circular rod under uniaxial tension. This case can be further extended to a hollow rod, which is analogous to an individual truss member. As shown in Fig. 3. 2a, a circular rod of radius R is subjected to a tensile force P along its axis, the model assumes a thin film of infinitesimal thickness d (shown in green in Fig. 3. 2) perfectly bonded to the bulk body's free surfaces [43]. The constitutive equations

of the bulk body and surface are respectively:

$$\sigma_{ij} = \lambda\, E_{kk}\, \delta_{ij} + 2\,\mu\, E_{ij} \qquad \tau_{ij} = \lambda_s\, \varepsilon_{kk}\, \delta_{ij} + 2\,\mu_s\, \varepsilon_{ij} \tag{3.10}$$

where σ_{ij}, τ_{ij} are the stress tensors of the bulk body and the surface respectively. E_{ij}, ε_{ij} are the strain tensors of the bulk body and the surface respectively. The surface Lame's constants λ_s, μ_s are different from those of the bulk body λ, μ.

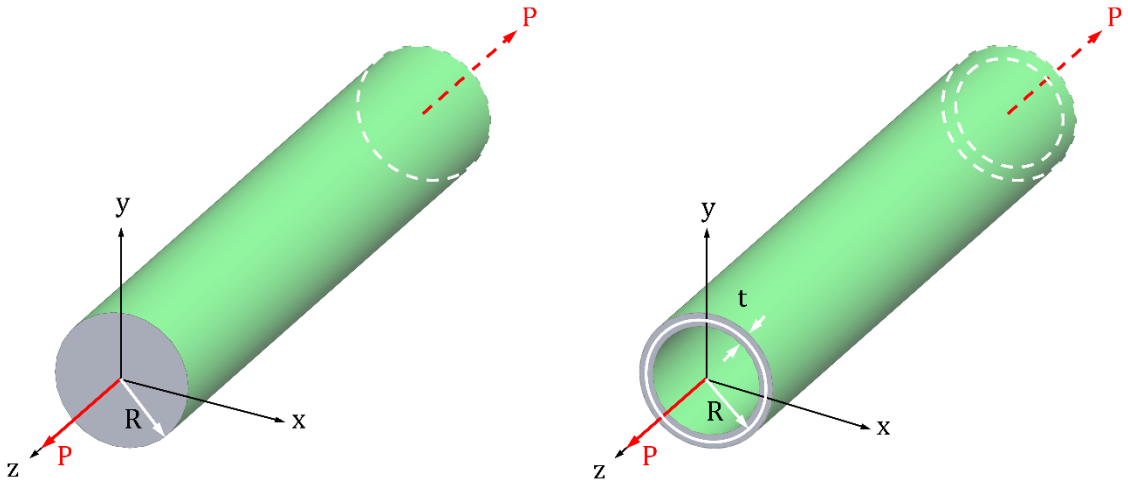

Fig. 3. 2 1D circular rod under a uniaxial tensile load P along the z direction: (a) solid, (b) hollow.

The stress tensors of the bulk body and the surface are respectively:

$$\sigma = \begin{bmatrix} \sigma_{11} & 0 & 0 \\ 0 & \sigma_{22} & 0 \\ 0 & 0 & \sigma_{33} \end{bmatrix} \qquad \tau = \begin{bmatrix} \tau_{11} & 0 & 0 \\ 0 & \tau_{22} & 0 \\ 0 & 0 & \tau_{33} \end{bmatrix} \tag{3.11}$$

The uniaxial loading constitutive equations can be further simplified as follows:

$$\sigma_{zz} = E_b\, E_{zz} \qquad \tau_{zz} = E_s\, \varepsilon_{zz} \tag{3.12}$$

where E_b, E_s are the elastic moduli of the bulk body and the surface respectively, and E_{zz}, ε_{zz}

are the uniaxial bulk body and surface strains in the z direction respectively.

The equilibrium condition of the rod under the applied load P is:

$$\int \sigma_{zz}\, d\Omega + \int \tau_{zz}\, ds = P \tag{3.13}$$

where $d\Omega, ds$ are the infinitesimal cross-sectional areas of the bulk body and the surface respectively. Since the thin film is assumed to be perfectly attached to the bulk body, they both experience the same strain for the case of a uniaxial tension along the z direction. The boundary condition can be expressed as follows:

$$E_{zz} = \varepsilon_{zz} = \varepsilon \tag{3.14}$$

From Eqs. 3.12 to 3.14, P can be related to the elastic moduli as follows:

$$P = [\pi\, R^2\, E_b + 2\pi\, R\, d\, E_s]\, \varepsilon \tag{3.15}$$

For a homogenous rod with effective elastic modulus E_f, P is described as:

$$P = \pi\, R^2\, E_f\, \varepsilon \tag{3.16}$$

From Eqs. 3.15 and 3.16, the effective elastic modulus E_f is related to the moduli of the bulk body and the surface E_b and E_s as follows:

$$E_f = E_b + \frac{2d}{R} E_s \tag{3.17}$$

which can be further simplified as follows:

$$\frac{E_f}{E_b} = 1 + \frac{R_c}{R} \tag{3.18}$$

where $R_c = 2d\ E_s/E_b$ is the critical radius. When the rod radius R approaches R_c, size effect starts to emerge, and for radii much greater than this value size effects are negligible. This relation forms what is known as a scaling law as shown in Fig. 3. 3.

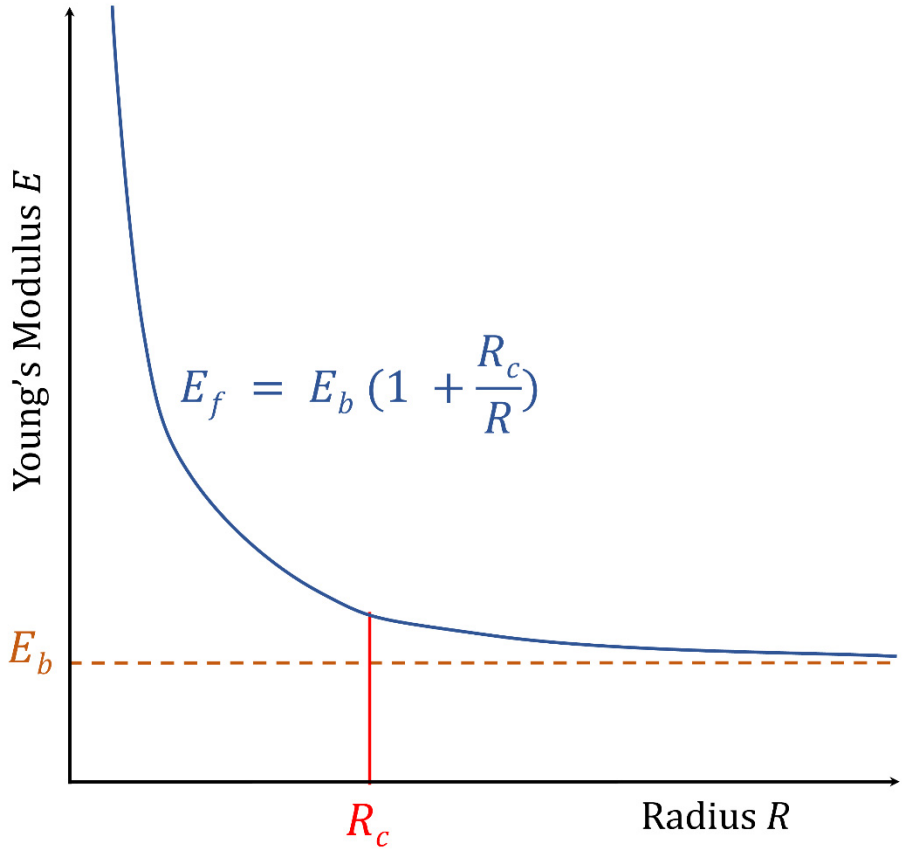

Fig. 3. 3 Scaling behavior for the case of 1D circular rod.

If we extend the above case to a 1D hollow rod of mean radius R and thickness t. In this case, the thin film is assumed to be attached to both the internal and external free surfaces. Eqs. 3.15 and 3.16 are modified as follows:

$$P = [2\pi\ R\ t\ E_b + 4\pi\ R\ d\ E_s]\ \varepsilon \tag{3.19}$$

$$P = 2\pi\ R\ t\ E_f\ \varepsilon \tag{3.20}$$

where the cross-sectional area of the hollow rod is approximated as $2\pi\ R\ t$.

Eqs. 3.17 and 3.18 for this case are as follows:

$$E_f = E_b + \frac{2d}{t} E_s \tag{3.21}$$

$$\frac{E_f}{E_b} = 1 + \frac{t_c}{t} \tag{3.22}$$

where $t_c = 2d\ E_s/E_b$ is the critical thickness.

Upon comparing R_c and t_c from the two cases of solid and hollow rods made from the same constituent material (i.e. have the same d, E_s, and E_b), it is evident that size effects are easily triggered in the hollow rod case rather than in the solid one in terms of how small dimensions should be. The reason is: (i) for the size effects to emerge in a solid rod, the radius should approach double the film thickness $2d/R$, (ii) while in the hollow rod case, they emerge when the thickness (not the radius) approaches double the film thickness $2d/t$. In conclusion, the emergence of size effects depends on the ratio of the free perimeter to the solid cross-sectional area perpendicular to the loading direction.

In order for the previously-derived continuum-based model to be representative of metamaterials at all lengthscales, the size effects can be included in the stiffness and compliance tensors by replacing the constituent material elastic modulus E_s with the effective elastic modulus E_f in Eqs 3.8 and 3.9 respectively.

The free perimeter to solid cross-sectional area ratio also results in an anisotropic characteristic as evident from the following discussion. Consider a square rod of side a and length L, under two different loading cases. The first case is a uniaxial tensile load P applied along the z direction as shown in Fig. 3. 4. The effective elastic modulus is related to the bulk and surface moduli as follows:

$$E_f = E_b + \frac{4d}{a} E_s \tag{3.23}$$

The second case is a uniaxial tensile load P applied along the y direction. The elastic moduli relation is as follows:

$$E_f = E_b + \frac{2(a+L)\,d}{a\,L} E_s \tag{3.24}$$

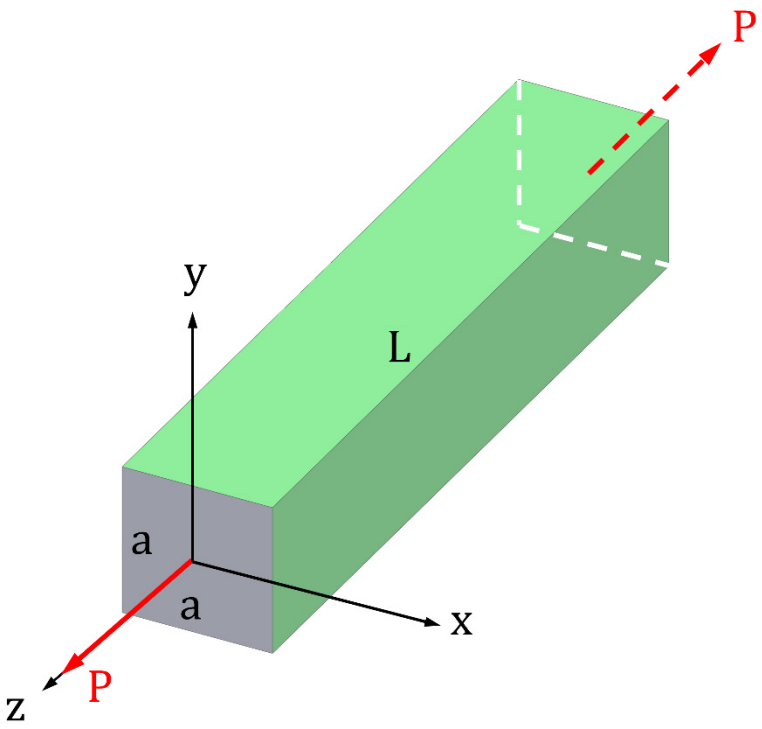

Fig. 3. 4 Square rod under a uniaxial tensile load P in the z direction.

Upon comparing Eqs. 3.23 and 3.24, it can be noted that a different effective elastic modulus exists for each loading case depending on the free perimeter to cross sectional area ratio perpendicular to the loading direction, which represents an anisotropic property of the "Gurtin Murdoch" surface elasticity model.

3.3. Conclusions

The constitutive model of the octet-truss lattice is extended to account for the lattice angle parameter. The pin-jointed nodes assumption is assumed as well as isotropic and homogeneous properties of the constituent material. The procedure for developing the continuum-based model can be summarized in these steps: (i) select the smallest substructure that composes the whole unit cell, a tetrahedron in this case, (ii) transform the individual truss members from their local coordinates to the unit cell's global coordinates, and (iii) apply homogenization and averaging procedures to relate the local stress-strain relation to the effective stress-strain relation. The resulting stiffness/compliance tensors depend on four main parameters: E_s the elastic modulus of the constituent material, A_c the cross-sectional area of the truss members, L the side length of the tetrahedron prism, and θ the lattice angle.

In order to fully represent octet-truss metamaterials using the developed stiffness/compliance tensors, it is important to include a parameter representing the size effects in the tensors. "Gurtin Murdoch" linearized theory of surface elasticity has been utilized to represent size effects using the effective elastic modulus E_f, which can replace the constituent material elastic modulus E_s in the macroscopic compliance/stiffness tensors.

Chapter 4 Impact of the Lattice Angle on The Effective Properties of The Octet-truss Lattice Structure

Summary: Due to its favorable stretching-dominated behavior, the octet-truss lattice has been studied extensively and continuum constitutive models have been developed to describe its effective mechanical properties. However, previous studies were only performed for the case of cubic symmetry where the lattice angle θ equals 45°. In this chapter, we studied the impact of the lattice angle on the effective properties of the octet-truss lattice, namely the relative density, effective stiffness, and effective strength. The relative density formula is extended to account for the lattice angle and results are compared with actual values obtained from CAD software. Tensor transformations are utilized to visualize the spatial distribution of the effective stiffness at different lattice angles. Analytical formulas are developed to obtain the loading direction and value of the maximum and minimum absolute as well as specific elastic moduli at different lattice angles. In addition, tridimensional orientation-dependent polar representations of the macroscopic strength of the octet-truss lattice are plotted for different lattice angles. Finally, collapse surfaces due to plastic yielding are introduced for two different loading combinations at different lattice angles.

4.1. Relative Density

The formula for the relative density of the octet-truss lattice could be extended to account

for the lattice angle parameter as follows:

$$\overline{\rho} = \frac{\pi r^2\left[\sqrt{2} + 2\,sec(\theta)\right]}{L^2\,tan(\theta)} - 39.97\,cos(\theta)^2\left(\frac{r}{L}\right)^3 \tag{4.1}$$

where r is the radius of the individual member and L is the base side length of the tetrahedron substructure. The first term in derived as the summation of the tetrahedron truss members' solid volume divided by the total tetrahedron volume. This term does not account for the volume shared at the nodes, hence it's only accurate for small aspect ratios.

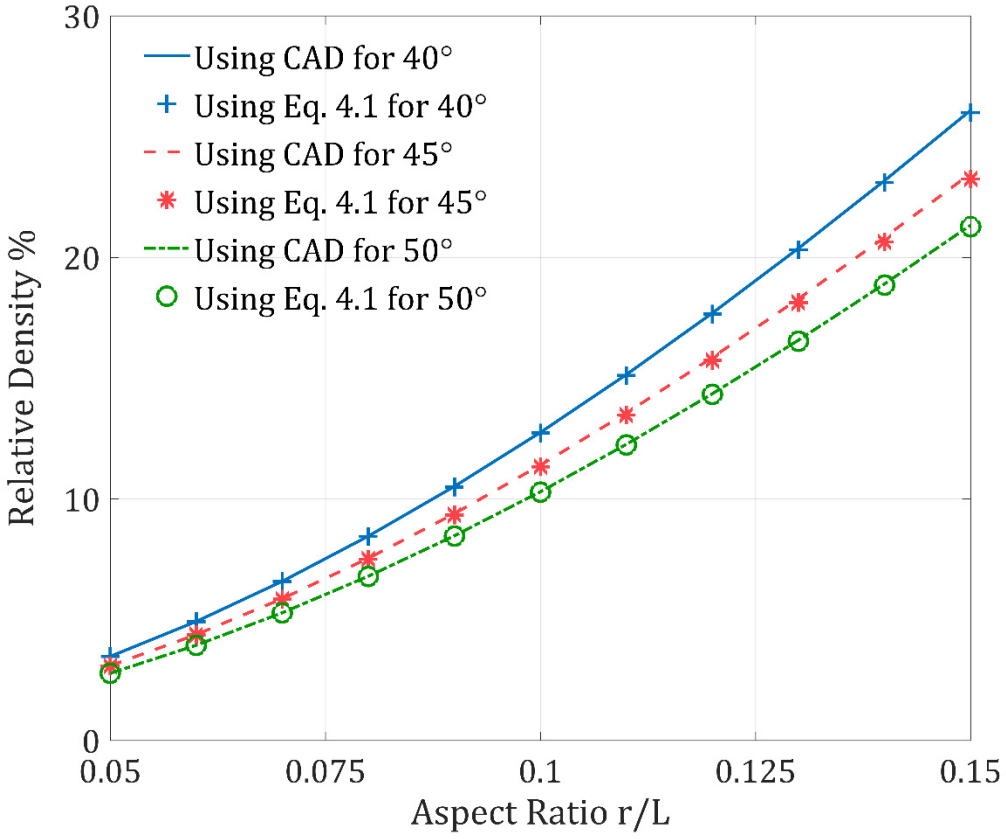

Fig. 4. 1 A comparison between relative density values using Eq. 4.1 vs CAD-extracted values at different lattice angles.

The second term includes a correction parameter that has been defined using curve fitting of relative density values extracted from a CAD model of the octet-truss lattice. It is worth

noting that Eq. 4.1 is only valid for cylindrical solid members. Developing a similar formula for hollow members proves to be more tedious because of the three different parameters existent in this case (i.e. aspect ratio, lattice angle, and thickness). Fig. 4. 1 shows percentage errors of relative density values using Eq. 4.1 vs CAD-extracted values for different lattice angles.

4.2. Effective Elastic Modulus

4.2.1. Compliance Tensor Transformations and Tridimensional Representations

To obtain $E''_{11} = 1/S''_{11}$, the effective elastic modulus in a general loading direction along x'' axis (defined by angles φ and α in Fig. 4. 2), two successive tensor transformations are applied analytically [44]. The transformed stress and strain vectors and compliance tensor are related to the original ones as follows:

$$\{\sigma_{xyz}\} = [T_1]\{\sigma'_{xyz}\} = [T_1][T_3]\{\sigma''_{xyz}\} \tag{4.2}$$

$$\{\varepsilon_{xyz}\} = [T_2]\{\varepsilon'_{xyz}\} = [T_2][T_4]\{\varepsilon''_{xyz}\} \tag{4.3}$$

$$[S''] = [T_4]^{-1}[S'][T_3] = [T_4]^{-1}[T_2]^{-1}[S][T_1][T_3] \tag{4.4}$$

where T_1 and T_2 are the first stress and strain transformation matrices between x, y, z and x', y', z', and T_3 and T_4 are the second stress and strain transformation matrices between x', y', z' and x'', y'', z''.

From Eq. 4.4, E''_{11} can be expressed as follows:

$$E_{11}'' = \left[\frac{cos(\alpha)^2\, sin(\alpha)^2}{cos(\theta)^2\, sin(\theta)} - \frac{sin(\alpha)^2\,[cos(\alpha)^2 + 1]}{\sqrt{2}\, tan(\theta)}\right.$$
$$+ \frac{sin(\alpha)^4\,[\sqrt{2}\, cos(\theta) + 1]}{2\, sin(\theta)^3}$$
$$- \frac{2\, cos(\alpha)^4\, sin(\theta)\, cos(\beta)^2\, sin(\beta)^2\,[1 - \sqrt{2}\, cos(\theta)^3]}{cos(\theta)^4} \quad (4.5)$$
$$\left. + \frac{cos(\alpha)^4\, sin(\theta)}{2\, cos(\theta)^4} + \frac{cos(\alpha)^4\, tan(\theta)}{\sqrt{2}}\right]^{-1}$$

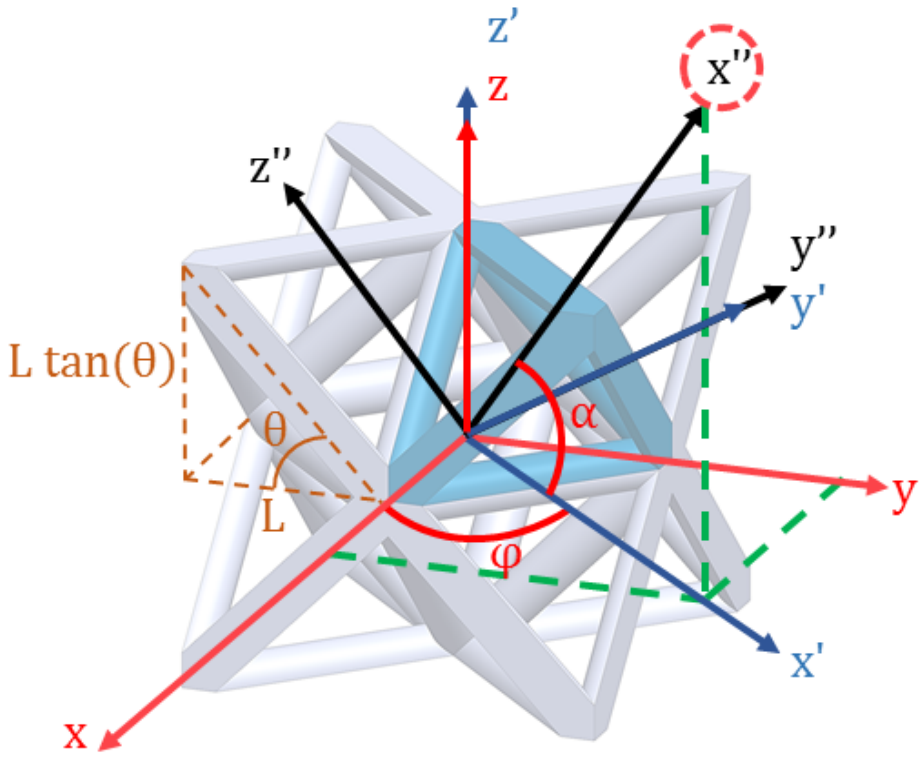

Fig. 4. 2 The octet-truss unit cell with the tetrahedron substructure geometry and the transformation coordinate systems.

Tridimensional orientation-dependent polar plots have been previously used to describe the anisotropy of monocrystallines [45–47]. The effect of the lattice angle on the effective elastic modulus of the octet-truss lattice can be visualized by generating such representations of E_{11}'' for three different lattice angles as can be seen in Fig. 4. 3.

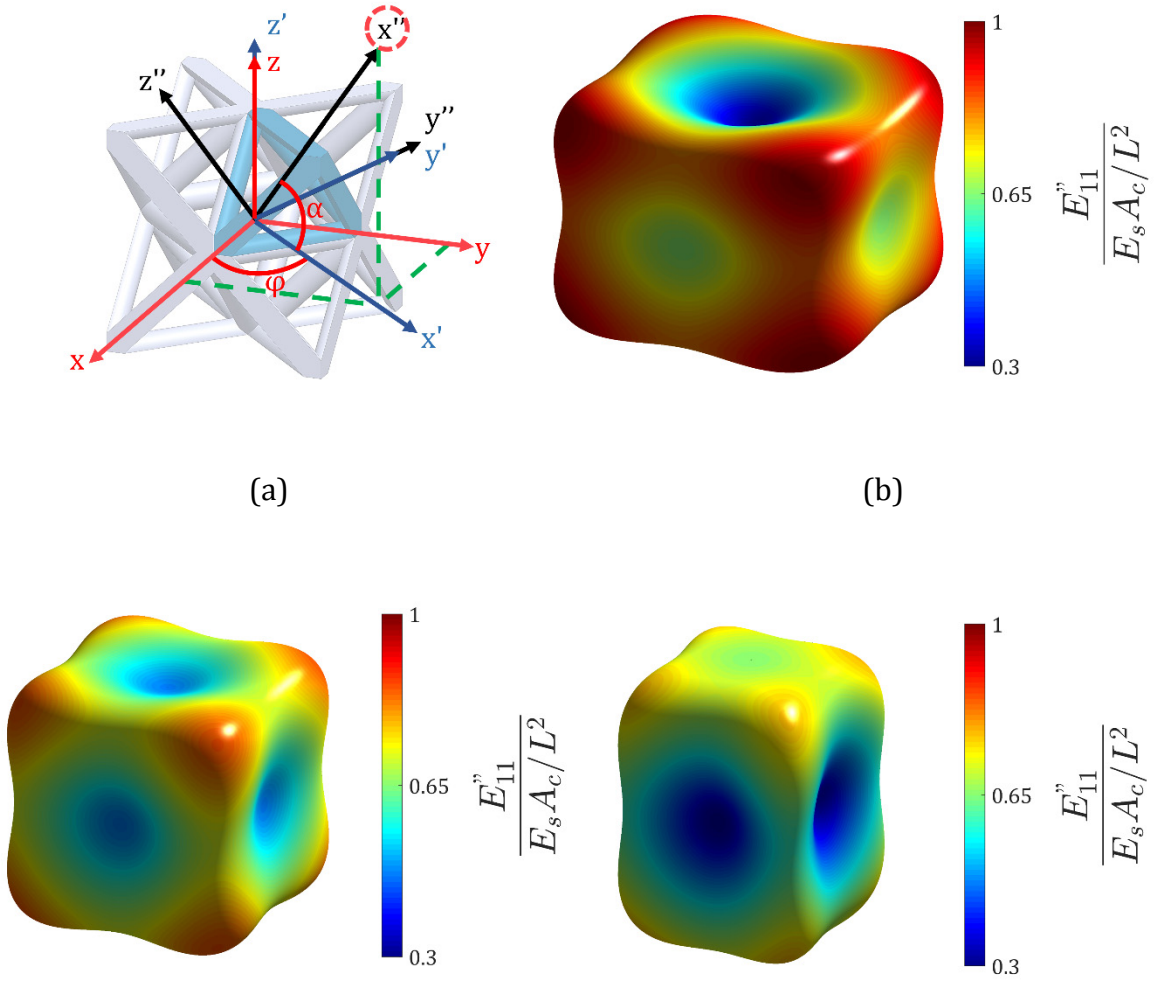

Fig. 4. 3 Tridimensional orientation-dependent polar representations of the effective elastic modulus for different lattice angles: (a) Orientation of the octet-truss unit cell, (b) For 40° lattice angle, (c) For 45° lattice angle, (d) For 50° lattice angle.

As can be noted, for the case of cubic symmetry (i.e. lattice angle $\theta = 45°$), the elastic modulus is equal in x, y, z directions. For lattice angles $\theta > 45°$, the elastic modulus in the z direction is greater than those in x and y directions and the opposite is true for lattice angles $\theta < 45°$.

4.2.2. Elastic Constants vs Lattice Angle

The maximum elastic modulus in the case of cubic symmetry coincides with the $\pm x = \pm y = \pm z$ line, which is aligned with the line connecting the tip of the tetrahedron to the octet-truss unit cell center. For lattice angles $\theta > 45°$, the maximum elastic modulus moves away from the $x - y$ plane and closer to the z direction, and the opposite is true for lattice angles $\theta < 45°$. It can also be noted that the maximum elastic modulus always lies on a plane perpendicular to the $x - y$ plane at $\varphi = (45 + 90n)°$, where n is an integer. This observation can simplify the analytical complexity of finding the value and direction of the maximum elastic modulus. Instead of solving a system of two equations (for a 3D surface), it can be simplified to one equation in one variable (for a 2D curve) by assuming $\varphi = 45°$ in Eq. 4.5 and differentiating E_{11}'' by the angle α as follows:

$$\begin{aligned}\frac{\partial E_{11}''}{\partial \alpha} = \big(&-8\cos(\alpha)\sin(\alpha)\sin(\theta)^3\cos(\theta)\\ &* \{2\cos(\alpha)^2 + 2\cos(\theta)^2 - 3\cos(\alpha)^2\cos(\theta)^2 + \sqrt{2}\cos(\theta)^3[2\cos(\alpha)^2 + 1]\\ &- 2\sqrt{2}\cos(\alpha)^2\cos(\theta)[\cos(\theta)^4 + 1] - 1\}\big)\\ &/\big(\cos(\theta)[3\cos(\alpha)^4 - 4\cos(\alpha)^2 + 1] + \sqrt{2}\cos(\alpha)^4\sin(\theta)^2[2 - \cos(\theta)^2]\\ &+ \sqrt{2}\cos(\theta)^4\big)^2\end{aligned} \tag{4.6}$$

The second derivative can be derived similarly. To find the angle α of the maximum elastic modulus, we solve $\partial E_{11}''/\partial\alpha = 0$. The angle α corresponding to the maximum point is as follows:

$$\alpha = \cos^{-1}\left(\sqrt{\frac{\sqrt{2}\cos(\theta)^3 + 2\cos(\theta)^2 - 1}{\sqrt{2}\cos(\theta)^5 - 2\sqrt{2}\cos(\theta)^3 + 3\cos(\theta)^2 + 2\sqrt{2}\cos(\theta) - 2}}\right) \tag{4.7}$$

For Eq. 4.7 to yield real values that correspond to the local maximum value of the elastic

modulus, the second derivative needs to be negative and the expression within the cosine inverse brackets should be a real number within the range of 0 to 1. By solving numerically, the range of valid values of θ is found to be $\theta < 53.59°$. In Fig. 4. 4, $cos(\alpha)^2$ is plotted against the lattice angle θ, from which it can be noted that: (i) For $53.59° < \theta < 67.59°$, Eq. 4.7 yields imaginary values of α, (ii) For $67.59° < \theta$, the second derivative is positive meaning the curve has no local maximum values, and its two extremes must be checked. To account for all lattice angles, the angle α of the maximum elastic modulus can be summarized as follows:

$$\alpha = \begin{cases} cos^{-1}\left(\sqrt{\dfrac{\sqrt{2}\,cos(\theta)^3 + 2\,cos(\theta)^2 - 1}{\sqrt{2}\,cos(\theta)^5 - 2\sqrt{2}\,cos(\theta)^3 + 3\,cos(\theta)^2 + 2\sqrt{2}\,cos(\theta) - 2}}\right) & \theta < 53.59° \\ 90° & 53.59° \leq \theta \end{cases} \tag{4.8}$$

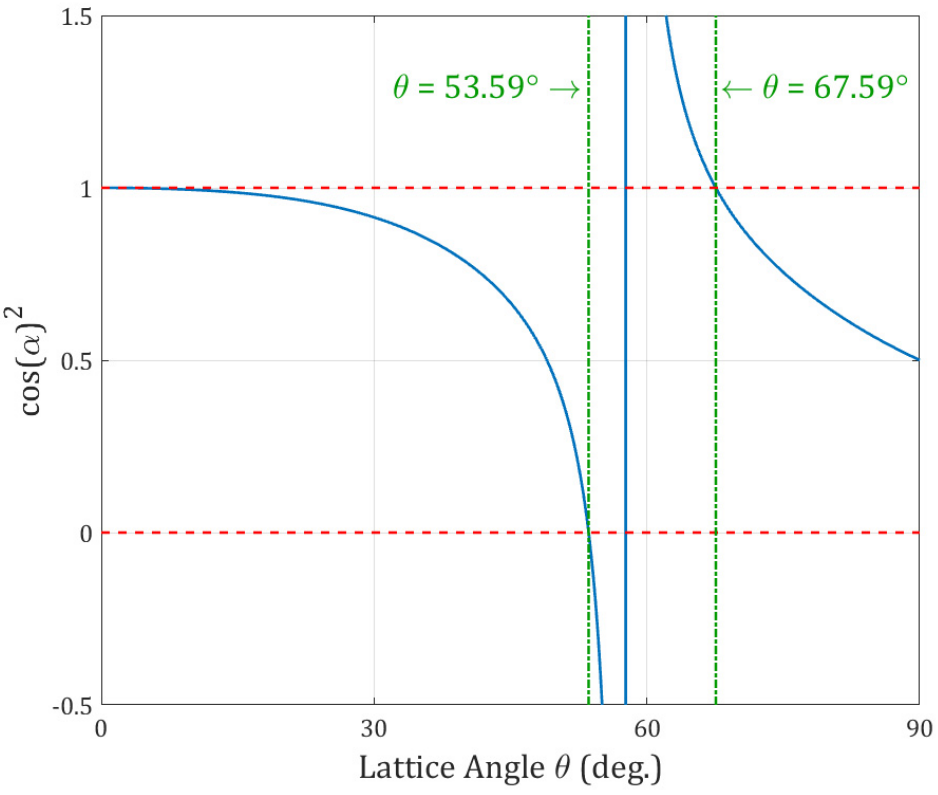

Fig. 4. 4 Behavior of $cos(\alpha)^2$ against the lattice angle θ.

At the micro and nano length scales, lattice angles outside the approximate range of 30°: 60° produce complex stress states at the nodes, which renders the mechanical behavior unpredictable and generally should be avoided. This was demonstrated by Montemayor and Greer (2015) for hollow members manufactured using two-photon lithography then sputtered with gold [28].

From Fig. 4. 3, it can be also noted that the loading direction of the minimum elastic modulus always coincides with one or more of the three orthogonal axes x, y, z as follows:

$$\textit{Loading direction of the lowest elastic modulus} \begin{cases} \theta > 45° & \textit{coincides with } x \textit{ and } y \textit{ axes} \\ \theta = 45° & \textit{coincides with } x, y \textit{ and } z \textit{ axes} \\ \theta < 45° & \textit{coincides with } z \textit{ axis} \end{cases} \tag{4.9}$$

Using Eq. 4.5, 4.8, and 4.9, the maximum and minimum elastic moduli and those along the x, y, z axes can be plotted against the lattice angle θ as shown in Fig. 4. 5.

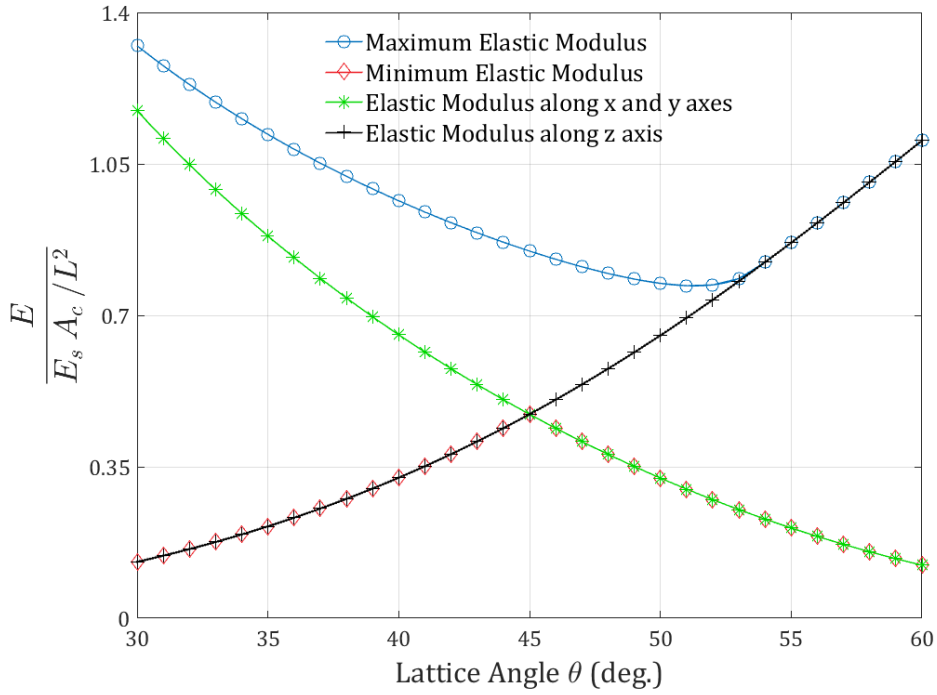

Fig. 4. 5 Elastic modulus behavior vs. the lattice angle θ.

It can be noted that the maximum elastic modulus is at a minimum at the lattice angle $\theta = 53.59°$, and increases as the lattice angle moves away from this value in either direction. As for the minimum elastic modulus, it's at a maximum at $\theta = 45°$ and decreases as we move away from cubic symmetry in either direction. At $\theta = 45°$, the octet-truss lattice is found to be at the minimum possible level of anisotropy, in other words the minimum difference between the maximum and minimum elastic moduli values. It's also at $\theta = 45°$ that the elastic moduli in $x,\ y,\ z$ directions are equal (i.e. cubic symmetry).

Another significant elastic constant is the shear modulus G. In Fig. 4. 6, the shear moduli in $y-z,\ x-z,\ x-y$ planes are plotted against the lattice angle θ.

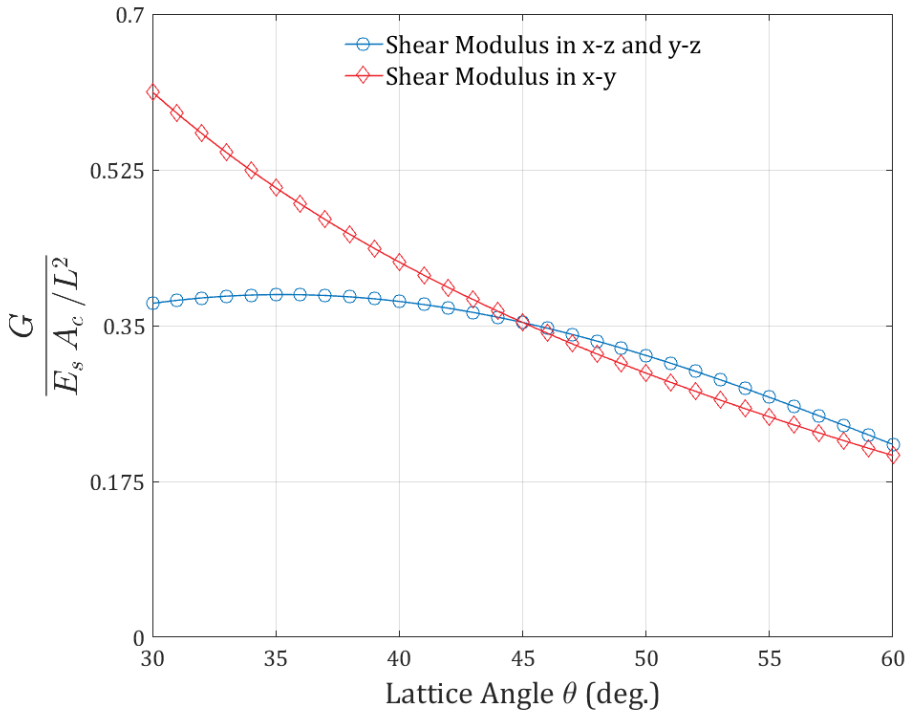

Fig. 4. 6 Shear modulus behavior vs. the lattice angle θ.

The cubic symmetry is achieved at $\theta = 45°$, where the shear moduli are equal in the three orthogonal planes. The $x-y$ plane seems to be a favorable loading plane when $\theta < 45°$ since

the shear modulus in $x-y$ as well as the elastic moduli in x and y directions increase as the lattice angle decreases.

A similar plot of Poisson's ratio is shown in Fig. 4. 7. Similarly, Poisson's ratio in the three orthogonal planes are equal for $\theta = 45°$. An interesting observation is that ν_{xz} (and by symmetry ν_{yz}) becomes greater than 1 as the lattice angle decreases below roughly 33.8°.

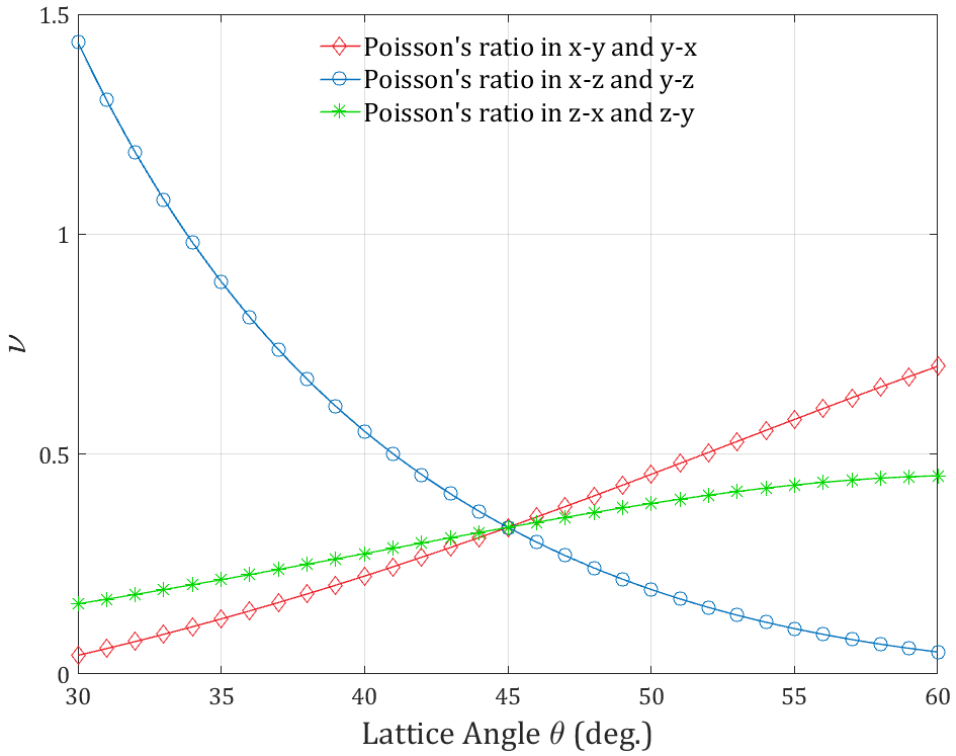

Fig. 4. 7 Poisson's ratio behavior vs. the lattice angle θ.

4.2.3. Specific Stiffness

For some engineering applications, specific stiffness bears more significance than absolute stiffness. The maximum specific stiffness is obtained by dividing the maximum elastic modulus by the relative density. The minimum specific stiffness is another significant quantity that helps understand the anisotropy level of the structure for different lattice

angles and aspect ratios. It's is obtained similarly to the maximum specific stiffness. Fig. 4. 8a shows the change in specific stiffness and percentage relative density with respect to the lattice angle for two different aspect ratios ($r/L = 0.05\ vs\ 0.1$).

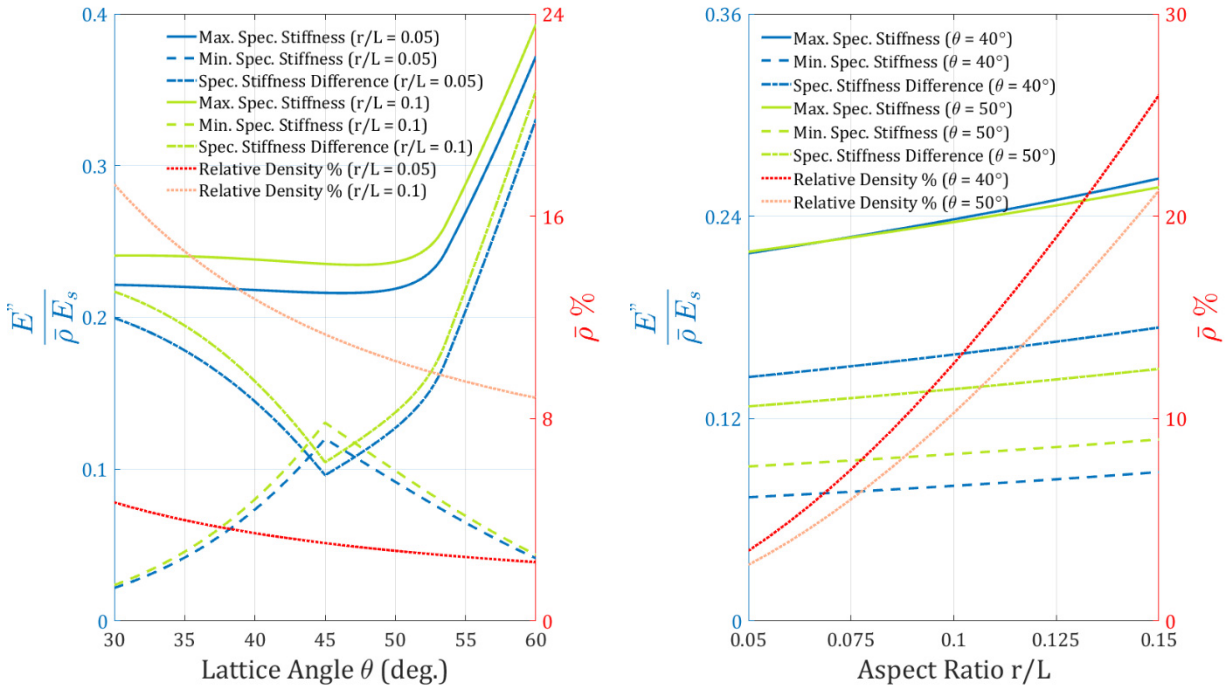

(a) (b)

Fig. 4. 8 Specific stiffnesses and percentage relative density of the octet-truss lattice: (a) With respect to the lattice angle θ for two aspect ratios r/L = 0.05 and 0.1, (b) With respect to the aspect ratio r/L for two lattice angles $\theta = 40°$ and 50°.

Specific stiffness values are divided by the constituent material elastic modulus in order to be only representative of the lattice geometry. It can be noted that the cubic symmetry case at $\theta = 45°$ is considered to be the least anisotropic for any aspect ratio, with the anisotropy level increasing as the lattice angle moves away from cubic symmetry. Specific stiffness is also noted to be slightly higher for the greater aspect ratio. An interesting observation is that

the maximum stiffness is almost constant with respect to changes in the lattice angle up till roughly 50° after which there is a sharp increase.

Fig. 4. 8b shows the change in specific stiffnesses and percentage relative density vs the aspect ratio r/L for two different lattice angles 40° and 50°. The maximum and minimum specific stiffnesses increase slightly as the aspect ratio increases.

4.3. Effective Strength

The macroscopic strength‡ of the octet-truss lattice is defined as the maximum stress the lattice can sustain without any of its members reaching a critical stress limit. This limit can be defined according to two main modes of failure: (i) yielding for ductile materials or fracture for brittle materials (tensile or compressive), and (ii) Euler beam buckling (compressive). An additional mode of failure for hollow-tube lattices is the shell buckling (compressive). Dominance of either one of these types depends on the loading conditions and the geometry of the lattice members, namely their aspect ratio and cross-section [27].

In order to relate the effective strength of the octet-truss lattice to the local strength of its individual members, the effective macroscopic strains are transformed from the global coordinates to the local member coordinates as follows:

$$\varepsilon^{(k)} = N_{ij}^{(k)}\,\bar{\varepsilon}_{ij} = n_i^{(k)} n_j^{(k)}\,\bar{\varepsilon}_{ij} \tag{4.10}$$

‡ Macroscopic stresses and strains are denoted by a bar sign above the symbol as in $\bar{\sigma}$ and $\bar{\varepsilon}$ respectively.

where $\varepsilon^{(k)}$ is the axial strain in the k^{th} member, $N_{ij}^{(k)}$ is a linear transformation operator that can be reduced to the product of the k^{th} member's direction cosines $n_i^{(k)}$ and $n_j^{(k)}$ (Fig. 3. 1b), and $\bar{\varepsilon}_{ij}$ is the macroscopic strain, which can be related to a general stress tensor $[\bar{\sigma}'']$ applied through a general direction defined by the angles φ and α (see Fig. 4. 2) through the following relation:

$$\{\bar{\varepsilon}_{ij}\} = [S]\,[T_1]\,[T_3]\,\{\bar{\sigma}''\} \tag{4.11}$$

By considering the tetrahedron substructure selected as the structural basis in the continuum-based model of the octet-truss, the stress in its six members can be expressed as follows:

$$\sigma^{(k)} = E_s\, n_i^{(k)}\, n_j^{(k)}\,[S]\,[T_1]\,[T_3]\,\{\bar{\sigma}''\} \tag{4.12}$$

where $\sigma^{(k)}$ is a stress vector of six components, one for each of the tetrahedron's truss members, $k = 1, 2 \ldots 6$ identifies the truss members, and $i, j = 1, 2, 3$ refer to the direction vector components.

4.3.1. Tridimensional Representations

Given a general macroscopic stress state, Eq. 4.12 outputs six stress values, one for each of the tetrahedron six members. For a safe loading state, the condition $\{\sigma^{(k)}\} < \sigma_{lim}$ should hold true.

Similar to the discussion of the effective elastic modulus, Eq. 4.12 can be employed to visualize the effective strength of the octet-truss under a uniaxial tensile/compressive stress applied through a general direction defined by the angles φ and α using tridimensional

orientation-dependent polar plots as shown in Fig. 4. 9.

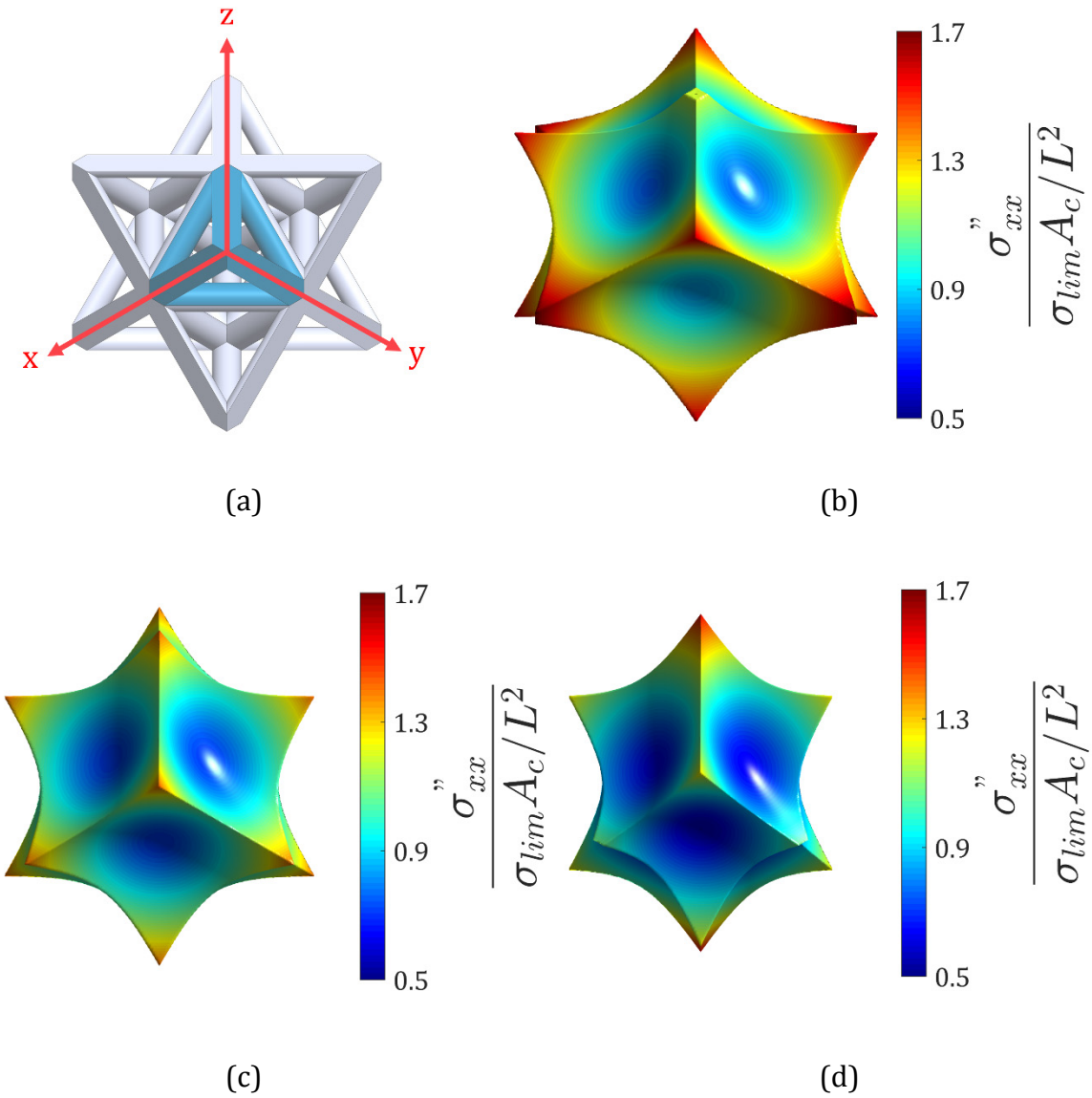

Fig. 4. 9 Tridimensional orientation-dependent polar representations of the effective strength for different lattice angles: (a) Orientation of the octet-truss unit cell, (b) For 40° lattice angle, (c) For 45° lattice angle, (d) For 50° lattice angle.

It can be noted that the direction of the maximum lattice strength $\bar{\sigma}_{max}$ for the cubic symmetry case of $\theta = 45°$ aligns with $\pm x, \pm y, \pm z$ axes in addition to the line $\pm x = \pm y = \pm z$

as can be shown in Fig. 4. 9c. As for $\theta < 45°$, the direction of $\bar{\sigma}_{max}$ aligns with $\pm x$ and $\pm y$ axes only[§]. For $\theta > 45°$, the direction of $\bar{\sigma}_{max}$ aligns with the $\pm z$ axis only.

4.3.2. Collapse Surfaces

The collapse surfaces of the octet-truss lattice due to plastic yielding are calculated for two combinations of loading, namely $(\bar{\sigma}_{zz}, \bar{\sigma}_{xz})$ and $(\bar{\sigma}_{xx}, \bar{\sigma}_{yy})$, for different lattice angles. The tetrahedron substructure is used in the analysis in both cases, along with the pin-jointed assumption employed in the continuum-based model of the octet-truss. The collapse surface for each combination of loads can be categorized into a number of modes depending on the governing collapse equation and which members would reach the yield stress σ_y for ductile materials (or fracture stress for brittle materials) with reference to Fig. 3. 1b.

4.3.2.1. Collapse surface in $(\bar{\sigma}_{zz}, \bar{\sigma}_{xz})$ space

The collapse surface under the applied loads $(\bar{\sigma}_{zz}, \bar{\sigma}_{xz})$ is shown in Fig. 4. 10 for three different lattice angles. In Modes Ia and Ib, member no. 2 has reached its yield stress σ_y (under compression in Mode Ia and tension in Mode Ib). The governing equations are as follows:

Mode Ia:
$$\frac{\bar{\sigma}_{xz}}{\sigma_y A_c/L^2} = \frac{1}{2\,tan(\theta)} * \frac{\bar{\sigma}_{zz}}{\sigma_y A_c/L^2} + cos(\theta) \tag{4.13}$$

[§] As can be noticed in Fig. 4.9b, the direction of $\bar{\sigma}_{max}$ doesn't perfectly align with x and y axes, it occurs a few degrees above and below the x-y plane. For example, at the lattice angle of $\theta = 40°$, the angles of $\bar{\sigma}_{max}$ are $\phi = n90°$ and $\alpha = \pm 1.92°$. However, the difference between $\bar{\sigma}_{max}$ and $\bar{\sigma}$ at x and y axes at $\theta = 40°$ is 0.3%.

Mode Ib: $$\frac{\bar{\sigma}_{xz}}{\sigma_y A_c/L^2} = \frac{1}{2\,tan(\theta)} * \frac{\bar{\sigma}_{zz}}{\sigma_y A_c/L^2} - cos(\theta) \quad (4.14)$$

As for Modes IIa and IIb, member no. 5 has reached its yield stress σ_y (under compression in Mode IIa and tension in Mode IIb). The governing equations are as follows:

Mode IIa: $$\frac{\bar{\sigma}_{xz}}{\sigma_y A_c/L^2} = \frac{-1}{2\,tan(\theta)} * \frac{\bar{\sigma}_{zz}}{\sigma_y A_c/L^2} - cos(\theta) \quad (4.15)$$

Mode IIb: $$\frac{\bar{\sigma}_{xz}}{\sigma_y A_c/L^2} = \frac{-1}{2\,tan(\theta)} * \frac{\bar{\sigma}_{zz}}{\sigma_y A_c/L^2} + cos(\theta) \quad (4.16)$$

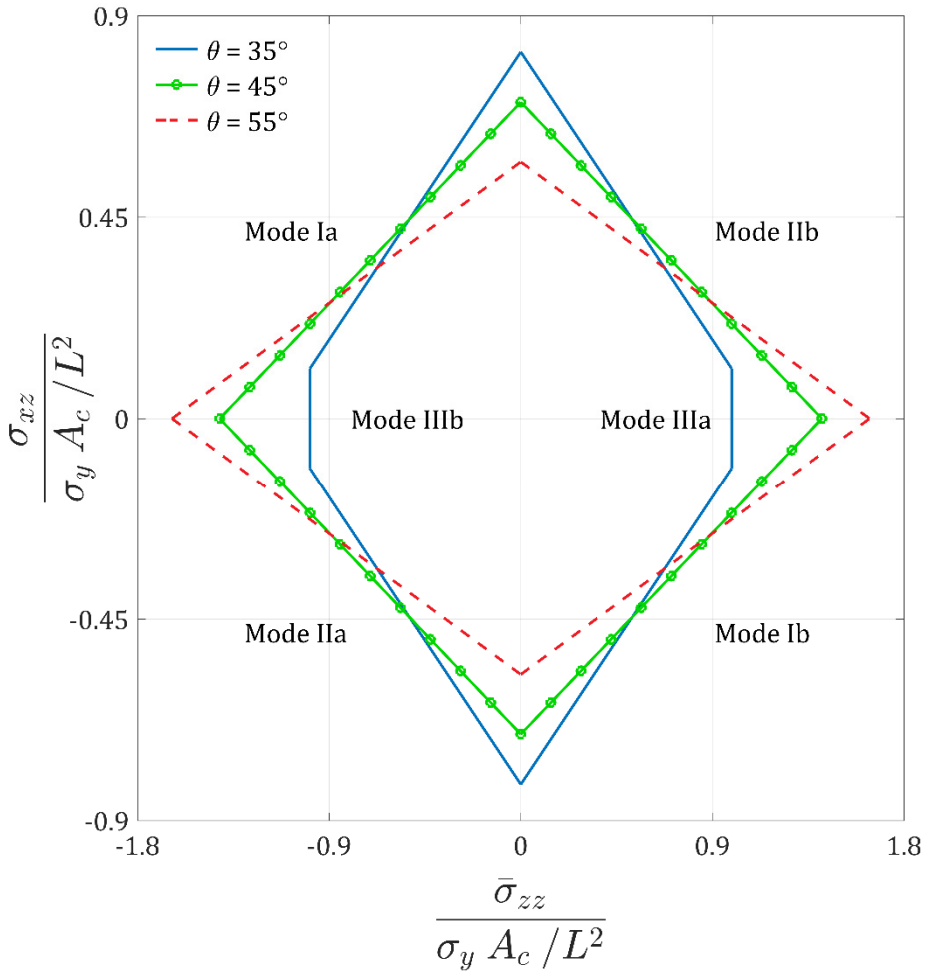

Fig. 4. 10 Collapse surface of the octet-truss due to plastic yielding in ($\bar{\sigma}_{zz}, \bar{\sigma}_{xz}$) space.

For lattice angles $\theta < 45°$, there exists two additional Modes, IIIa and IIIb, where members

no. 1 and 4 have reached their yield stress σ_y (under compression in Mode IIIa and tension in Mode IIIb). The governing equations are as follows:

Mode IIIa: $$\frac{\bar{\sigma}_{zz}}{\sigma_y A_c/L^2} = +\sqrt{2}\,tan(\theta) \tag{4.17}$$

Mode IIIb: $$\frac{\bar{\sigma}_{zz}}{\sigma_y A_c/L^2} = -\sqrt{2}\,tan(\theta) \tag{4.18}$$

4.3.2.2. Collapse surface in $(\bar{\sigma}_{xx}, \bar{\sigma}_{yy})$ space

The collapse surface under the applied loads $(\bar{\sigma}_{xx}, \bar{\sigma}_{yy})$ is shown in Fig. 4. 11.

In Modes IVa and IVb, members no. 2, 3, 5 and 6 have reached their yield stress σ_y (albeit 2 and 5 are under tension and 3 and 6 are under compression in Mode IVa and the opposite in Mode IVb).

The governing equations are as follows:

Mode IVa: $$\frac{\bar{\sigma}_{yy}}{\sigma_y A_c/L^2} = \frac{\bar{\sigma}_{xx}}{\sigma_y A_c/L^2} + \frac{2\,cos(\theta)}{tan(\theta)} \tag{4.19}$$

Mode IVb: $$\frac{\bar{\sigma}_{yy}}{\sigma_y A_c/L^2} = \frac{\bar{\sigma}_{xx}}{\sigma_y A_c/L^2} - \frac{2\,cos(\theta)}{tan(\theta)} \tag{4.20}$$

As for Modes Va and Vb, members no. 1 and 4 have reached their yield stress σ_y (under compression in Mode Va and under tension in Mode Vb). The governing equations are as follows:

Mode Va: $$\frac{\bar{\sigma}_{yy}}{\sigma_y A_c/L^2} = \frac{-\bar{\sigma}_{xx}}{\sigma_y A_c/L^2} - \frac{\sqrt{2}}{tan(\theta)} \tag{4.21}$$

Mode Vb: $$\frac{\bar{\sigma}_{yy}}{\sigma_y A_c/L^2} = \frac{-\bar{\sigma}_{xx}}{\sigma_y A_c/L^2} + \frac{\sqrt{2}}{tan(\theta)} \tag{4.22}$$

Upon comparison, the collapse surfaces at the lattice angle of $\theta = 45°$ under the two loading combinations of $(\bar{\sigma}_{zz}, \bar{\sigma}_{xz})$ and $(\bar{\sigma}_{xx}, \bar{\sigma}_{yy})$ clearly agree with those developed by Deshpande et al. (2001) in both shape and value [8].

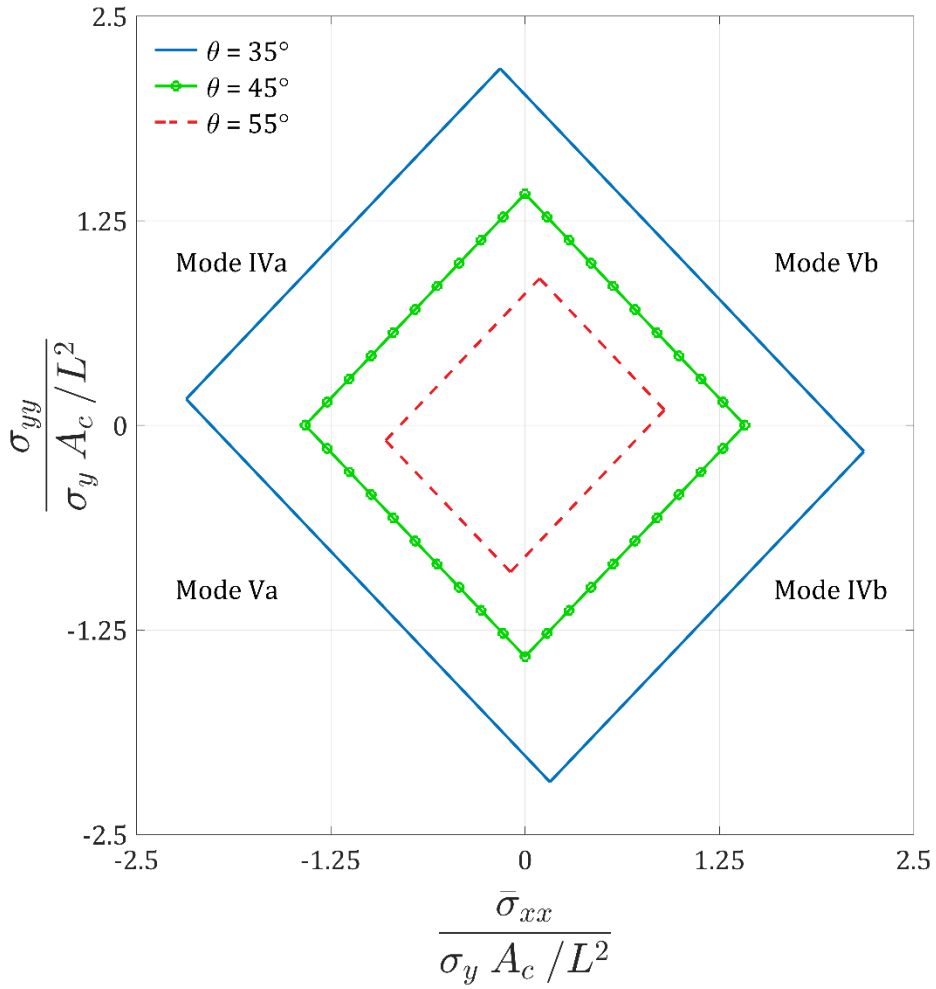

Fig. 4. 11 Collapse surface of the octet-truss due to plastic yielding in $(\bar{\sigma}_{xx}, \bar{\sigma}_{yy})$ space.

4.4. Conclusions

The purpose of this chapter was to investigate the effect of the lattice angle on the effective properties of the octet-truss lattice structure. The relative density formula of the octet-truss

lattice was extended to account for the lattice angle via curve-fitting of CAD-extracted values. The resultant equation produced accurate results upon comparison with actual values from CAD software. A general expression for the elastic modulus of the octet-truss for a general loading direction and a general lattice angle was obtained using tensor transformations. Tridimensional orientation-dependent polar representations of the elastic modulus for different lattice angles showed the loading direction of the maximum elastic modulus to always lie in a plane perpendicular to the $x - y$ plane at $\varphi = 45°$. As the lattice angle increases, this direction moves closer to the z axis. As it decreases, it moves closer to the $x - y$ plane. The elastic modulus expression was used to obtain analytical formulas for the loading direction angles of the maximum and minimum elastic moduli. A plot of the maximum and minimum specific stiffnesses against the lattice angle described the anisotropic behavior of the octet-truss lattice. The macroscopic strength behavior was demonstrated through tridimensional orientation-dependent polar representations for a general loading direction at different lattice angles. Plastic yielding collapse surfaces were developed for two different loading combinations along with the governing equations to illustrate the impact of the lattice angle on the effective strength of the octet-truss lattice.

Chapter 5 Numerical and Experimental Application: Lattice Structure Optimization

Summary: In the first section of this chapter, finite element modeling of the octet-truss lattice is performed in order to identify the effects of mesh selection and boundary conditions, as well as assess its accuracy by comparing the resulting elastic moduli values with those obtained using the continuum-based analytical model. Due to the high-symmetry of the octet-truss lattice, only the tetrahedron substructure is considered in the finite element analyses while applying the proper symmetry conditions. The lattice members' cross-sectional area is modeled as circular solid in the analyses, nonetheless hollow cross-sections of any shape are also valid.

Recent advances in additive manufacturing technologies have simplified the implementation of lattice structures for different applications, such as mechanical load-carrying components and energy-absorption, among others. Hence, lattice structure optimization (LSO) is gaining more attention recently. In the second section of this chapter, LSO in the commercial software HyperWorks by Altair, Inc. is evaluated in comparison to a continuum-based analytical model of the octet-truss lattice to assess its optimization efficiency. Comparison samples are verified using finite element analysis and further validated using stereolithography-based 3D printing and mechanical testing. Furthermore, recommendations are made for LSO in HyperWorks in order to increase its optimization efficiency and the user convenience.

5.1. Finite Element Model (3D vs 1D elements)

Three different mesh elements are employed: 3D solid, 1D beam, and 1D truss elements. The same parameter matrix varying the lattice angle and the aspect ratio is followed for every mesh element type used. Aspect ratios between 0.02 and 0.12 and lattice angles between 30 and 60 degrees were analyzed. In this context, the aspect ratio is defined as the ratio of the individual lattice member radius to its length $r/\sqrt{2}L$. The base side length of the tetrahedron (L in Fig. 3. 1b) is fixed, while the height of the tetrahedron changes with the lattice angle and the diameter of individual member is changed to obtain different aspect ratios.

Firstly, in order to assess the validity of the pin-jointed nodes assumption (i.e. neglecting the bending resistance of the nodes and members), the octet-truss lattice is modeled using 3D solid elements, which are capable of capturing member and node bending resistance in addition to the tensile/compressive and torsional stiffness of the lattice members. Secondly, 1D beam elements were employed to assess the effect of the bending of the lattice members on the macroscopic stiffness. Finally, 1D truss elements were utilized where only the tensile/compression stiffness of the lattice members is considered. It's worth noting that the torsional stiffness of the members is only significant when there exists asymmetry at the common nodes, a possible phenomenon in microfabrication [16].

A certain force F is applied on the tetrahedron substructure along the z axis, and the displacement is extracted from the FEA model. The elastic modulus is then calculated as the ratio of stress to strain per Eq. 5.1, where the stress is the force divided by the projected area and the strain is the displacement divided by the original height.

$$E_{lattice} = \frac{F \times Height}{L^2 \times Displacement} \quad (5.1)$$

5.1.1. Mesh Selection

For the case of 3D solid elements, a tetrahedral mesh was generated using HyperMesh. It was manually-refined until the displacement converged, with a final average mesh density of roughly 40,000 elements per cubic millimeter. Various quality parameters need to be checked to measure how far these elements deviate from the ideal shape of a tetrahedral elements, which is an equilateral tetrahedron. The most important of these quality parameters is the Jacobian, which has an ideal value of 1.0 and is recommended to be greater than 0.5. The Jacobian value was found to be above 0.5 for more than 99.9% of the tetrahedral elements, which gives a proper indication of the mesh quality [48].

For the case of 1D elements, a single element was applied to each of the tetrahedron members since the cross-section is constant. Care was given to the orientation of the half-cylinder cross-section of the beam in the case of 1D beam elements so that the bending resistance of the members is correctly simulated.

5.1.2. Boundary Conditions

Based on the assumption that the only contribution to the macroscopic elastic stiffness is from the elastic uniaxial tensile/compressive stiffness of the individual members, attention should be given to how the boundary conditions are defined in each case of the FEA model [8,30,39,49]. In the case of 3D solid elements, all the nodes on the upper surface were linked together through rigid elements (RBE2) with the compression force applied to the

independent node. The nodes on the bottom surface were constrained from translation in z direction and free to move in the x and y directions. Precautions were taken to maintain the symmetry conditions and to prevent rigid body movement of the model. Fig. 5. 1 shows the original vs deformed shape of the tetrahedron substructure. In the case of 1D elements, the boundary conditions are applied directly to the individual nodes. Fig. 5. 2 shows the original vs deformed shape of a full octet-truss unit cell with 1D truss elements.

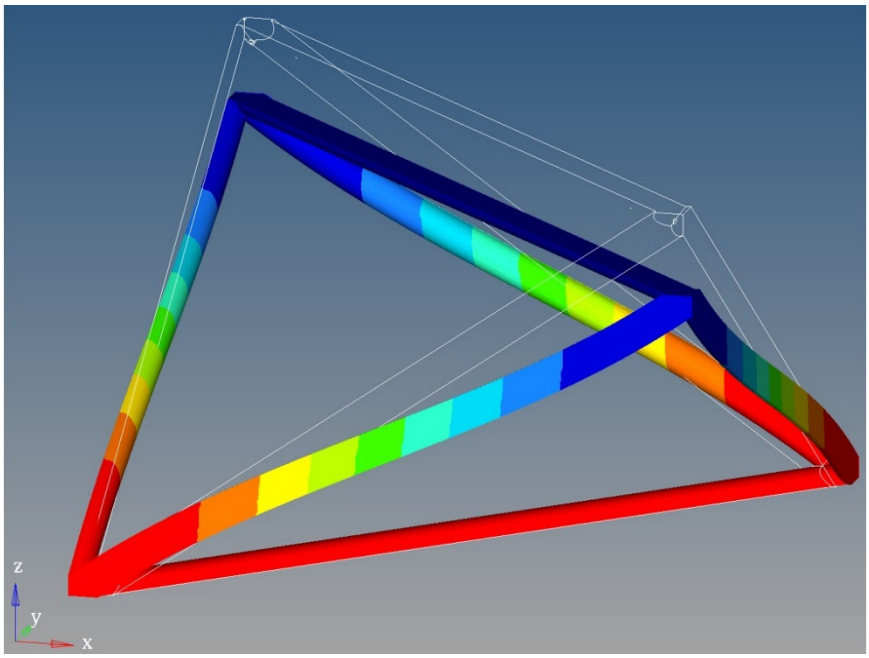

Fig. 5. 1 The deformed vs original shape of the tetrahedron model under a compressive force along the z direction. Colors represent displacement in the z direction.

5.1.3. Results

Elastic moduli values were calculated per the continuum-based analytical model, and compared to those obtained from the FEA for each geometrical configuration.

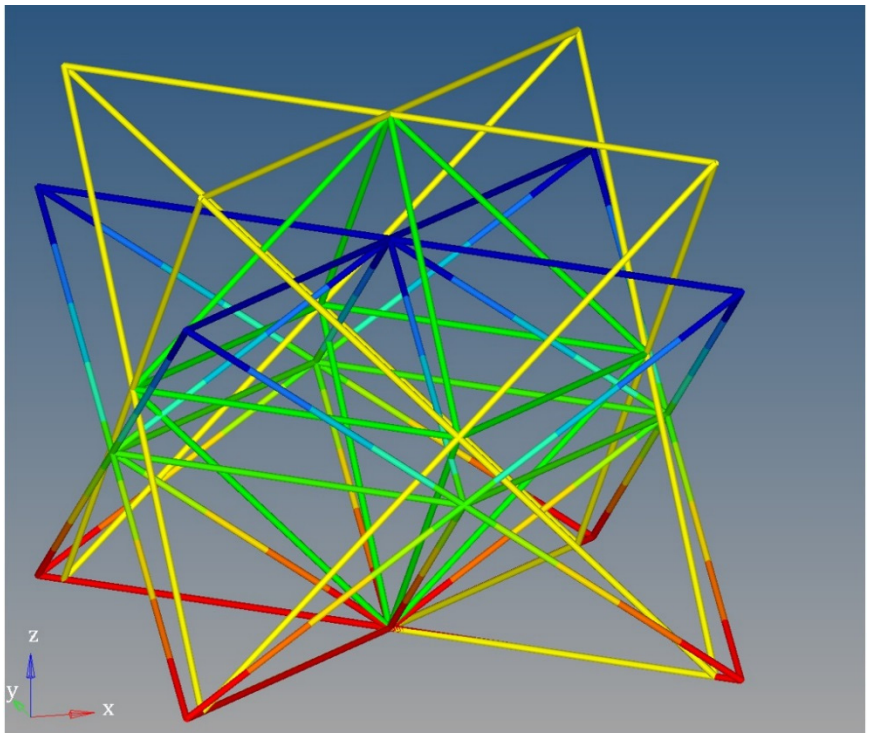

Fig. 5. 2 An octet-truss unit cell before and after deformation under a compressive force. Yellow represents the unit cell before deformation, and gradient colors represent the displacement value in the z direction.

For the 3D solid elements, elastic moduli demonstrated errors as high as 50% for the 0.12 aspect ratio, and lower error values for smaller aspect ratios. For the case of 0.02 aspect ratio and 60° lattice angle the error was found to be around 4%. This is mainly because the bending contribution from nodes and member to the overall stiffness of the structure is higher for large aspect ratios and small lattice angles (i.e. more solid material at the nodes) than for small aspect ratios and large lattice angles.

For the case of 1D beam elements, the elastic moduli values were more consistent with a maximum error of 7%, which is mainly due to the bending resistance of the tetrahedron members. As for the case of 1D truss elements, the simulations showed accurate results with less than 1% error. This is because this case completely aligns with the assumptions followed

in developing the continuum-based analytical model.

The choice of which FEA model to follow depends on the nature of the structure and application. For space structures, the aspect ratio is usually low and the cross-section is hollow, hence using the 1D element is justified. This is also the case for mechanical metamaterials; the main differences are that the dimensions are usually at the nano and micro length scales and the constituent material's mechanical properties are different.

For structural geometries of high aspect ratio, the 3D solid elements can produce more accurate results albeit at higher computational costs. Altair Engineering, Inc. recently included lattice structure optimization within their HyperWorks software package. It uses 1D tapered beam elements to represent lattice structure elements, which can't be reliably used for high aspect ratios.

It's worth noting that the highest stresses are found to be around the nodes. Although the continuum-based model can be utilized to investigate the macroscopic strength of lattice structures, it only considers the failure of the members (elastic buckling or plastic yielding). Hence, a correction parameter needs to be introduced to account for the plastic yielding at the nodes.

In the next section, we utilize the analytical model and FE simulation results in assessing the lattice structure optimization efficiency of the commercial software HyperWorks.

5.2. Lattice Structure Optimization in Altair HyperWorks

Lattice structure optimization (LSO) has been introduced recently in the software package

HyperWorks by Altair. It enables the creation of blended solid and lattice structures [48]. HyperWorks uses 1D tapered beam elements to represent the individual members of the lattice structure. LSO is inherently similar to topology optimization, albeit the design domain can now include intermediate density elements. LSO is carried out in two main phases: (i) Regular topology optimization is performed first with reduced penalty options in order to retain more intermediate density elements (Fig. 5. 3). At the end of phase I, these elements are replaced with lattice structures such that the volume fraction of the lattice structure corresponds to the intermediate element density. (ii) Size optimization is then performed to define the diameters of each element so that the homogenized lattice properties correspond to the initial intermediate element stiffness. Some anisotropy is integrated in the lattice structure during phase II in order to increase efficiency. An important remark about LSO in HyperWorks is that each initial mesh element is replaced with a single unit cell, hence the size, orientation and lattice angle are dependent upon the initial model mesh [48].

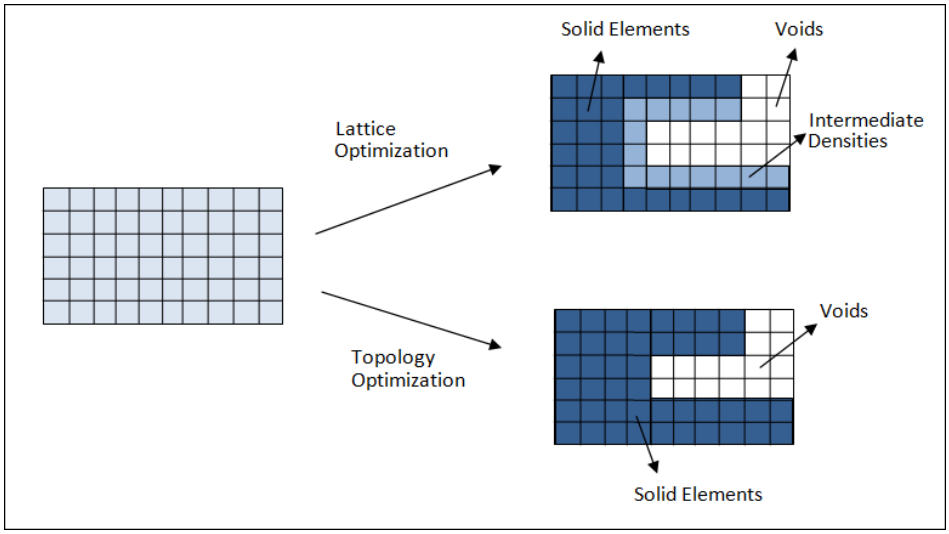

Fig. 5. 3 Difference between Lattice Optimization (Phase I) and Topology Optimization (Image courtesy of Altair).

In this section of the chapter, LSO in the commercial software Altair's HyperWorks is

evaluated in comparison to a continuum-based analytical model of the octet-truss lattice to assess its optimization efficiency. In the next subsection, the 3D printing and mechanical testing equipment are discussed in order to pinpoint the limitations and considerations to be accounted for when defining the problem employed to compare HyperWorks LSO to the continuum-based analytical model.

5.2.1. Experimental Setup

Form 2.0, a stereolithography-based 3D printer by Formlabs Inc., was utilized to produce sample lattice structures using a proprietary material called Tough with a reported elastic modulus of 1.7 GPa for the green part without additional treatments. Form 2.0 requires the addition of support material to the manufactured part, the distribution and size of which can be controlled within their software [50]. The minimum available layer thickness of 50 μm was used to obtain the most geometrically-accurate results. Sample octet-truss structures were manufactured using this 3D printer (Fig. 5. 4) to check the suitable range of member diameters and support material settings.

In order to check the validity of this 3D printer as a manufacturing platform for the problem specimens, we needed to ensure the material properties were consistent in all directions. Hence, ASTM D638-14 Type IV tension samples were manufactured in three orthogonal directions [51]. These samples were subjected to destructive tensile tests on MTS C43 Universal Testing System. Testing results showed inconsistency in the elastic modulus values for different directions rendering Form 2.0 unreliable for such purpose, albeit the tensile strength showed more consistency. However, given the high quality and the low cost of the printed samples, Form 2.0 can be used for demonstration purposes.

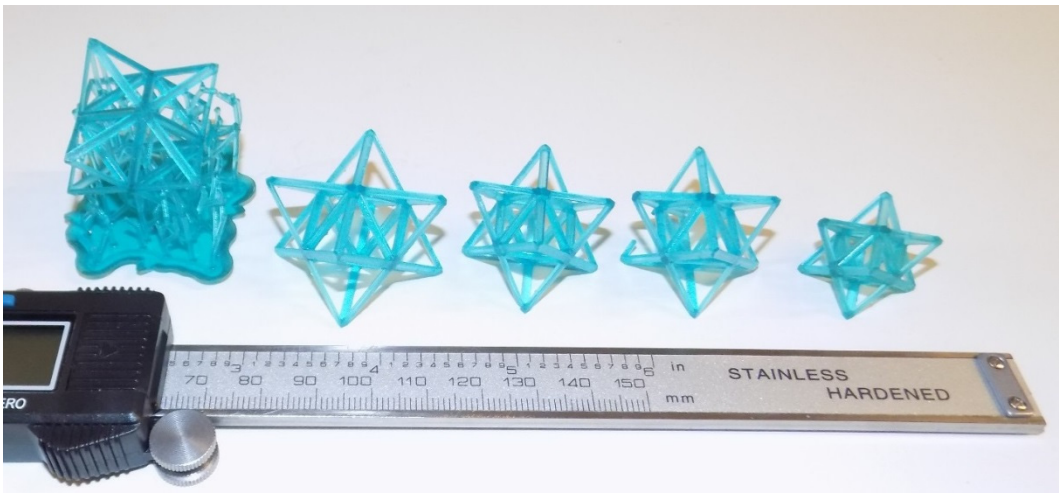

Fig. 5. 4 Octet-truss samples using Form 2.0, unit cell width $15 - 25mm$, members diameter 2mm, lattice angle $45° - 50°$. Support material is still attached to the leftmost lattice.

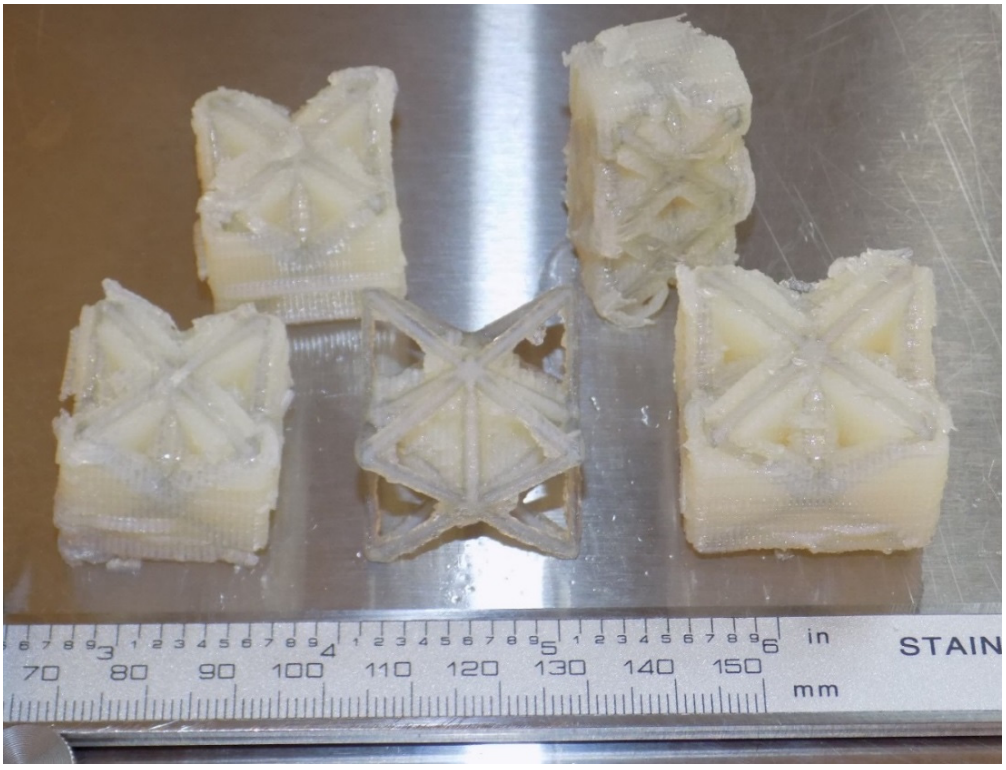

Fig. 5. 5 Octet-truss samples using Objet260, unit cell width $15 - 25mm$, members diameter $2mm$, lattice angle $40° - 45°$. Support material is partially removed.

Another 3D printer was utilized, Objet260 Connex3 by Stratasys. This printer implements a process called "PolyJet 3D Printing", where the printer head jets drops of curable photopolymer onto a build tray, which are subsequently cured using UV radiation. A proprietary material called Digital ABS was used, with a reported elastic modulus of 2.6 – 3.0 GPa [52]. Objet260 requires the use of support material, which could be removed later using water jetting. Similarly to Form 2.0, sample octet-truss structures were manufactured to investigate the appropriate settings that would produce the highest quality (Fig. 5. 5).

Fig. 5. 6 Right: Compression test setup on MTS C43 showing a laser extensometer, overhead light, and a video camera. A close-up of the cylindrical compression platens with the sample in place is shown in the top right corner. Left: Tension test setup. A close-up of the tension grips with the sample in place is shown in the top left corner.

ASTM D638-14 Type IV samples were manufactured in three orthogonal directions. Tensile testing experiments showed consistent results, with a mean elastic modulus of 2.3 GPa and a standard deviation of 0.08 GPa which is within the ranges suggested in ASTM D638-14 [51]. A laser extensometer was utilized to achieve high accuracy with reflective tapes attached to the top and bottom cylindrical platens as shown in the compression testing setup in Fig. 5. 6. Given that this is a compression test and the polymer test material has a much

lower elastic modulus than the machine building materials, the crosshead should give accurate displacement readings as well. The 3D printing and mechanical testing considerations for the problem definition can be summarized as follows: (i) The suitable member diameter should be $1.5 - 3\ mm$ in order to obtain the finest 3D printing quality without unnecessary costs, and (ii) The sample compressed area should not exceed a square of $20\ \times\ 20\ mm$.

5.2.2. Problem Definition and Analytical Results

For HyperWorks, the input geometry is a square rod with dimensions of $71.5\ \times\ 20\ \times 20$ mm. These dimensions were selected to enable meshing with three hexahedral elements at a lattice angle $\theta\ =\ 50°$. LSO was performed on this sample to generate lattice structure that would achieve the lowest volume fraction for a certain displacement ΔL under a certain compressive force F. The elastic modulus of the resultant lattice structure can be calculated per Eq. 5.2:

$$E_{lattice}\ = \frac{F\ \times\ 71.5}{\Delta L\ \times\ 20\ \times\ 20} \tag{5.2}$$

The resultant lattice structure is shown in Fig. 5. 7. It's worth noting that HyperWorks applied fixed boundary conditions (BC's) to the uppermost and lowermost nodes of the structure while leaving the middle nodes free to move in all directions. To simulate these BC's in the compression experiment, two plates of $2\ mm$ thickness were added at the top and bottom of the structure as shown in Fig. 5. 7.

The compliance tensor from the continuum-based model was used to generate a similar lattice structure for comparison. The same input geometry and material properties were

used to obtain the elements' diameter for the same elastic modulus from LSO. A multiplier had to be introduced into the compliance tensor equation to account for the difference in defining the BC's in the analytical model (see Section 5.1.2) and HyperWorks. Similarly, two plates were added at the top and bottom of the structure to simulate the same BC's in the compression test.

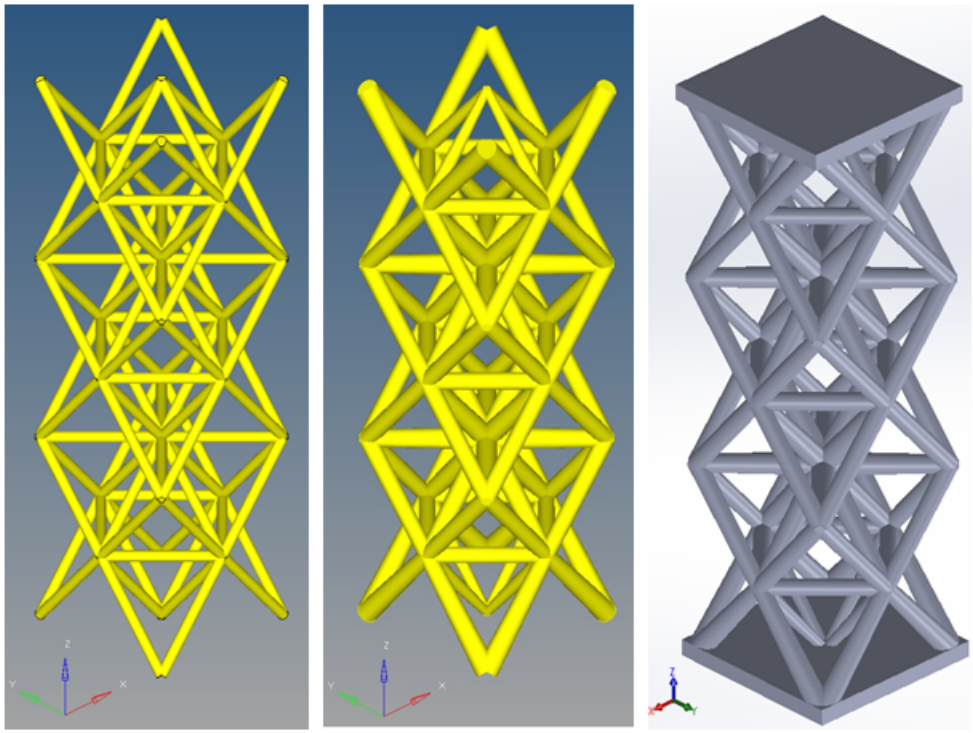

Fig. 5. 7 Lattice structure using HyperWorks' LSO after phase I (left), elements' radii range of 0.56-1.35 mm after phase II (center), and CAD model for 3D printing (right).

5.2.3. Compression Testing Results

The volumes of the two structures (analytical model vs HyperWorks) were calculated through SolidWorks and were found to be almost the same. Given the same input mesh geometry, HyperWorks and the analytical model can perform at the same level of efficiency. The two structures were manufactured using the Objet260 3D printer as shown in Fig. 5. 8.

Fig. 5. 8 Lattice structures generated using analytical model vs HyperWorks' LSO. Left: before removing support material (HyperWorks is left). Right: after removing support material (HyperWorks is bottom).

Cyclic compression testing of the two structures resulted in an elastic modulus of 55.8 MPa for HyperWorks vs. 62.4 MPa for the analytical model, with a percentage error of 10.6%. A possible explanation for this error could be the size/scaling effects in 3D printed polymers, in other words elements of different diameters have different mechanical properties. To investigate this phenomenon, a $2-mm$ diameter tension sample was manufactured using the Objet260 and mechanically tested. The mechanical behavior was significantly different from the standard Type IV sample as shown in Fig. 5. 9. The $2-mm$ diameter sample showed more ductility and strain hardening, and lower elastic modulus and tensile strength than the standard Type IV sample. Further extensive experimentation is required to fully characterize this phenomenon.

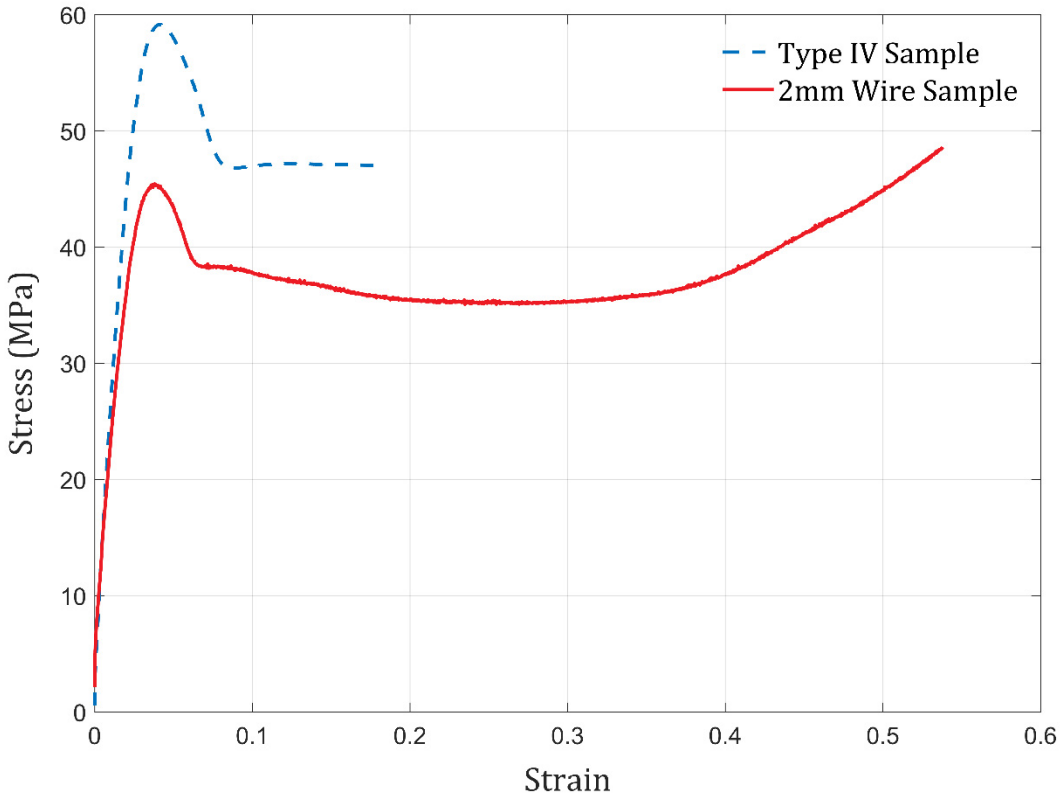

Fig. 5. 9 Mechanical behavior of standard Type IV specimen vs 2 mm diameter sample under tension.

With reference to the elastic modulus discussion in Chapter 4, it is possible to obtain higher stiffness using the same lattice geometry (member geometry and lattice angle) by changing the loading direction. However, for the sake of consistency the same loading direction was used in both the analytical model and LSO samples. Two main recommendations can be made at this stage concerning LSO in HyperWorks: (i) Decoupling the lattice unit cell size from the mesh element size proves to be more efficient. Mesh element size is dependent upon the complexity of geometry and the degree of output accuracy required from the FEA. On the other hand, lattice unit cell size depends on other considerations such as the limitations of the fabrication process. (ii) Decouple the orientation of the lattice unit cell from that of the mesh element. It has been proven in Chapter 4 that loading along the x, y, or z

directions does not guarantee the maximum stiffness, hence it is essential that more freedom be given in selecting the optimum loading direction of the output lattice structure.

5.3. Conclusions

5.3.1. Finite Element Modeling

In comparison with the continuum-based analytical model of the octet-truss, 3D solid elements along with 1D truss/beam elements were utilized. The 1D truss elements were found to be the most accurate with respect to the macroscopic elastic modulus of the structure since it completely aligns with the continuum-based model assumptions. However, for geometries with high aspect ratios, the analytical model tends to produce higher errors. For small aspect ratios, it is advised to use 1D beam/truss elements to represent lattice structures given the computational cost saving associated with 1D over 3D elements. Although both 1D elements capture accurate displacement values (i.e. structural stiffness), accurate stress analysis can only be performed using 3D solid elements.

5.3.2. Lattice Structure Optimization

LSO in HyperWorks is performed in two phases, topology optimization then size optimization. Comparison between LSO in HyperWorks with the analytical model showed that they can perform on the same level of optimization given the same input geometry. Decoupling the lattice unit cell size and orientation from those of the initial mesh size could potentially increase the optimization efficiency and the user convenience of HyperWorks' Lattice Structure Optimization. Objet260 3D printed samples demonstrated size/scaling

effects, different mechanical behavior for different sample sizes. However, the analytical model vs HyperWorks comparison still holds as it was verified using finite element analysis.

Chapter 6 Conclusions and Future Work

In this chapter, we state the problem, identify the objectives of the research and outline the contributions resulting from the work. Furthermore, a brief description of potential future work is presented.

6.1. Statement of the Problem

Architectural materials refer to materials consisting of a unit cell tessellated in three orthogonal directions to form a network or a lattice structure. In the last few decades, they have successfully demonstrated being suitable candidates for lightweight load-carrying structures. With the advent of size effects observed in some classes of materials when their dimensions are scaled down to the micro and nano lengthscales, the new field of mechanical metamaterials came to light.

Mechanical metamaterials combine the benefits of low density, as they are fundamentally hollow structures, with high stiffness and strength, via the utilization of size effects combined with structural effects (i.e. the arrangement of their individual elements in the best possible configuration to carry the loads). One of the best candidate unit cells for such application is the octet-truss. Although there have been several studies on the octet-truss's effective properties, they were all performed in early 2000s and before. At that time, applications other than mechanical metamaterials were is mind, such as space structures and sandwich panels. Consequently, the literature ignored important parameters affecting the effective

properties of the octet-truss such as the lattice angle θ and the loading direction. With the huge potential demonstrated by metamaterials, it is imperative to fully characterize the properties of the octet-truss lattice. Efficiently optimizing the structural configuration of the octet-truss, combined with favorable size effects, would unlock the full capacity of mechanical metamaterials in applications such as mechanical structures and energy absorption.

In this study, the effective properties of the octet-truss lattice were studied while accounting for the different lattice angles and loading directions.

6.2. Objectives

The objective of this work is to fully describe the effective properties of the octet-truss lattice at different lattice angles. Special care was given to:

(i) Analytical derivation of the stiffness/compliance tensors of the octet-truss lattice while including the lattice angle parameter θ.

(ii) Mathematically-modeling the size effects of metamaterials in the stiffness/compliance tensors of the octet-truss.

(iii) Extending the relative density formula of the octet-truss to include the lattice angle parameter up to a higher-order approximation.

(iv) Describing the effective stiffness of the octet-truss lattice and illustrating its variation with the lattice angle and loading direction. In addition, analytical

formulas were derived to calculate the value and direction of the maximum and minimum elastic moduli at different lattice angles.

(v) Studying the effective strength of the octet-truss lattice under a general loading condition and demonstrating spatial distribution using tridimensional representations and collapse surfaces.

(vi) Demonstrating the potential of utilizing the octet-truss's effective properties in lattice structure optimization via a comparison with commercial optimization software. This is a crucial step towards fully unlocking the potential of metamaterials.

6.3. General Conclusions

The objective of this study was to fully describe the effective properties of the octet-truss lattice, and demonstrate the potential of utilizing this knowledge in structurally-optimizing the lattice for different loading conditions. The general conclusions can be summarized as follows:

6.3.1. Derivation of the Stiffness/Compliance Tensors

In this work, the appropriate steps were followed to develop a continuum-based analytical model of the octet-truss lattice while including the lattice angle parameter θ. The output of these analytical derivations were the stiffness/compliance tensors. Isotropic and homogenous properties were assumed for the constituent material. The pin-jointed nodes assumption was assumed to simplify the derivations, where we only considered the axial

compressive/tensile stiffness of the truss members and ignored the nodes and members bending resistance. This assumption aligns with the stretching-dominated behavior of the octet-truss.

6.3.2. Effective Stiffness

Two consecutive tensor transformations were utilized to obtain an analytical expression of the effective stiffness from a general loading conditions. Tridimensional orientation-dependent polar representations were employed to spatially-describe the distribution of the octet-truss's effective stiffness. Maximum and minimum as well as specific stiffness values were studied against changes in the lattice angle and aspect ratio to demonstrate their impact.

6.3.3. Effective Strength

The effective strength of the octet-truss was developed as the maximum stress the lattice can sustain without any of its truss members reaching the limit stress. The effective strength formulations were later utilized to visualize the spatial strength under a general tensile/compressive load using tridimensional representations. In addition, collapse surfaces were plotted for different loading conditions along with the governing equations describing the failure criteria for each mode of collapse.

6.3.4. Application: Lattice Structure Optimization

The potential of utilizing the octet-truss's effective properties in lattice structure optimization was demonstrated via a comparison with the commercial software OptiStruct

by Altair, Inc. The analytical model was employed to calculate the dimensions of a sample with a given elastic modulus against another sample generated by OptiStruct, the weight of the sample was measured as the determining factor of optimization efficiency. These samples were later 3D printed and mechanically tested to experimentally demonstrate the potential of lattice structure optimization.

6.4. Future Work

The following points lay the foundations for future work on the same topic:

(i) Assuming different cross-sectional areas for different groups of parallel members could potentially provide higher optimization efficiency as opposed to assuming the same cross-sectional area for all of the octet-truss members.

(ii) Developing a systematic approach for the utilization of the octet-truss in lattice structure optimization instead of manually refining the properties would prove to be of much use in numerical optimization solutions.

References

1. Fleck, NA., Deshpande, VS., and Ashby, MF. 2010, "Micro-architectured materials: past, present and future", *Proc R Soc A Math Phys Eng Sci*, Vol(466), pp. 2495-2516.

2. Montemayor, LC., Meza, LR., and Greer, JR. 2014, "Design and Fabrication of Hollow Rigid Nanolattices via Two-Photon Lithography", *Adv Eng Mater*, Vol(16), pp. 184-189.

3. Zheng, X., Lee, H., Weisgraber, TH., Shusteff, M., DeOtte, J., Duoss, EB., Kuntz, JD., Biener, MM., Ge, Q., Jackson, J a., Kucheyev, SO., Fang, NX., and Spadaccini, CM. 2014, "Ultralight, ultrastiff mechanical metamaterials.", *Science*, Vol(344), pp. 1373-1377.

4. Lakes, R. 1993, "Materials with structural hierarchy", *Nature*, Vol(361), pp. 511-515.

5. Montemayor, L., Chernow, V., and Greer, JR. 2015, "Materials by design: Using architecture in material design to reach new property spaces", *MRS Bull*, Vol(40), pp. 1122-1129.

6. Gibson, LJ., and Ashby, MF. 1997, *Cellular Solids: Structure and Properties*, Cambridge University Press, Cambridge.

7. Deshpande, VS., Ashby, MF., and Fleck, NA. 2001, "Foam topology: bending versus stretching dominated architectures", *Acta Mater*, Vol(49), pp. 1035-1040.

8. Deshpande, VS., Fleck, NA., and Ashby, MF. 2001, "Effective properties of the octet-truss lattice material", *J Mech Phys Solids*, Vol(49), pp. 1747-1769.

9. Ashby, MF., Evans, T., Fleck, N., Hutchinson, JW., Wadley, HNG., and Gibson, LJ. 2000, *Metal Foams: A Design Guide*, Butterworth-Heinemann, Oxford.

10. Greer, JR., Oliver, WC., and Nix, WD. 2005, "Size dependence of mechanical properties of gold at the micron scale in the absence of strain gradients", *Acta Mater*, Vol(53), pp. 1821-1830.

11. Greer, JR., and Nix, WD. 2005, "Size dependence of mechanical properties of gold at the sub-micron scale", *Appl Phys A*, Vol(80), pp. 1625-1629.

12. Wang, J., Lian, J., Greer, JR., Nix, WD., and Kim, K-S. 2006, "Size effect in contact compression of nano- and microscale pyramid structures", *Acta Mater*, Vol(54), pp. 3973-3982.

13. Uchic, MD., Dimiduk, DM., Florando, JN., and Nix, WD. 2004, "Sample Dimensions Influence Strength and Crystal Plasticity", *Science (80-)*, Vol(305), pp. 986 LP-989.

14. Uchic, MD., Shade, PA., and Dimiduk, DM. 2009, "Plasticity of Micrometer-Scale Single Crystals in Compression", *Annu Rev Mater Res*, Vol(39), pp. 361-386.

15. Jang, D., and Greer, JR. 2010, "Transition from a strong-yet-brittle to a stronger-and-ductile state by size reduction of metallic glasses", *Nat Mater*, Vol(9), pp. 215-219.

16. Jang, D., Meza, LR., Greer, F., and Greer, JR. 2013, "Fabrication and deformation of three-dimensional hollow ceramic nanostructures.", *Nat Mater*, Vol(12), pp. 893-898.

17. Lian, J., Jang, D., Valdevit, L., Schaedler, TA., Jacobsen, AJ., B. Carter, W., and Greer, JR. 2011, "Catastrophic vs Gradual Collapse of Thin-Walled Nanocrystalline Ni Hollow

Cylinders As Building Blocks of Microlattice Structures", *Nano Lett*, Vol(11), pp. 4118-4125.

18. Gu, XW., Loynachan, CN., Wu, Z., Zhang, Y-W., Srolovitz, DJ., and Greer, JR. 2012, "Size-dependent deformation of nanocrystalline Pt nanopillars.", *Nano Lett*, Vol(12), pp. 6385-6392.

19. Rys, J., Valdevit, L., Schaedler, TA., Jacobsen, AJ., Carter, WB., and Greer, JR. 2014, "Fabrication and Deformation of Metallic Glass Micro-Lattices", *Adv Eng Mater*, Vol(16), pp. 889-896.

20. Jacobsen, AJ., Barvosa-Carter, W., and Nutt, S. 2007, "Micro-scale Truss Structures formed from Self-Propagating Photopolymer Waveguides", *Adv Mater*, Vol(19), pp. 3892-3896.

21. Jacobsen, AJ., Barvosa-Carter, W., and Nutt, S. 2008, "Micro-scale truss structures with three-fold and six-fold symmetry formed from self-propagating polymer waveguides", *Acta Mater*, Vol(56), pp. 2540-2548.

22. Torrents, A., Schaedler, TA., Jacobsen, AJ., Carter, WB., and Valdevit, L. 2012, "Characterization of nickel-based microlattice materials with structural hierarchy from the nanometer to the millimeter scale", *Acta Mater*, Vol(60), pp. 3511-3523.

23. Schaedler, TA., Jacobsen, AJ., Torrents, A., Sorensen, AE., Lian, J., Greer, JR., Valdevit, L., and Carter, WB. 2011, "Ultralight Metallic Microlattices", *Science (80-)*, Vol(334), pp. 962-965.

24. Bauer, J., Hengsbach, S., Tesari, I., Schwaiger, R., and Kraft, O. 2014, "High-strength cellular ceramic composites with 3D microarchitecture.", *Proc Natl Acad Sci U S A*, Vol(111), pp. 2453-2458.

25. Meza, LR., and Greer, JR. 2013, "Mechanical characterization of hollow ceramic nanolattices", *J Mater Sci*, Vol(49), pp. 2496-2508.

26. Meza, LR., Zelhofer, AJ., Clarke, N., Mateos, AJ., Kochmann, DM., and Greer, JR. 2015, "Resilient 3D hierarchical architected metamaterials.", *Proc Natl Acad Sci U S A*, Vol(112), pp. 11502-11507.

27. Meza, LR., Das, S., and Greer, JR. 2014, "Strong, lightweight, and recoverable three-dimensional ceramic nanolattices", *Science (80-)*, Vol(345), pp. 1322-1326.

28. Montemayor, LC., and Greer, JR. 2015, "Mechanical response of hollow metallic nanolattices: combining structural and material size effects", *J Appl Mech*, Vol(82), pp. 1-10.

29. Mikulas, M. M., J., Bush, HG., and Card, MF. 1977, *Structural Stiffness, Strength and Dynamic Characteristics of Large Tetrahedral Space Truss Structures*,

30. Nayfeh, AH., and Hefzy, MS. 1978, "Continuum modeling of three-dimensional truss-like space structures", *AIAA J*, Vol(16), pp. 779-787.

31. Heki, K. 1968, "On the effective rigidities of lattice plates", *Recent Res Struct Mech*,pp. 31-46.

32. Lake, MS. 1992, "Stiffness and strength tailoring in uniform space-filling truss

structures", *Nasa Tech Pap 3210*,pp. 1-28.

33. Wallach, JC., and Gibson, LJ. 2001, "Mechanical behavior of a three-dimensional truss material", *Int J Solids Struct*, Vol(38), pp. 7181-7196.

34. Wallach, JC., and Gibson, LJ. 2001, "Defect sensitivity of a 3D truss material", *Scr Mater*, Vol(45), pp. 639-644.

35. Hyun, S., Karlsson, AM., Torquato, S., and Evans, AG. 2003, "Simulated properties of Kagome and tetragonal truss core panels", *Int J Solids Struct*, Vol(40), pp. 6989-6998.

36. Christensen, RM. 2000, "Mechanics of cellular and other low-density materials", *Int J Solids Struct*, Vol(37), pp. 93-104.

37. Challapalli, A., and Ju, J. 2014, "Continuum Model for Effective Properties of Orthotropic Octet-Truss Lattice Materials", *Volume 9: Mechanics of Solids, Structures and Fluids*, ASME, Montreal, Canada.pp. V009T12A051.

38. Doyoyo, M., and Wanhu, J. 2006, "Plastic failure analysis of an auxetic foam or inverted strut lattice under longitudinal and shear loads", *J Mech Phys Solids*, Vol(54), pp. 1479-1492.

39. Wan Hu, J., and Park, T. 2013, "Continuum Models for the Plastic Deformation of Octet-Truss Lattice Materials Under Multiaxial Loading", *J Eng Mater Technol*, Vol(135), pp. 0210041-0210049.

40. Meza, LR. 2016, "Design, Fabrication, and Mechanical Property Analysis of 3D Nanoarchitected Materials",

41. Ru, CQ. 2010, "Simple geometrical explanation of Gurtin-Murdoch model of surface elasticity with clarification of its related versions", *Sci China Physics, Mech Astron*, Vol(53), pp. 536-544.

42. Dingreville, R., and Qu, J. 2005, "Surface free energy and its effect on the elastic behavior of nano-sized particles, wires and films", *J Mech Phys Solids*, Vol(53), pp. 1827-1854.

43. Eremeyev, VA. 2015, "On effective properties of materials at the nano- and microscales considering surface effects", *Acta Mech*, Vol(227), pp. 29-42.

44. Herakovich, CT. 1998, *Mechanics of Fibrous Composites*, Wiley, New York.

45. Xu, S., Shen, J., Zhou, S., Huang, X., and Xie, YM. 2016, "Design of lattice structures with controlled anisotropy", *Mater Des*, Vol(93), pp. 443-447.

46. Meyers, MA., and Chawla, K k. 2009, *Mechanical Behavior of Materials*, Cambridge University Press, Cambridge.

47. Nye, JF. 1985, *Physical Properties of Crystals : Their Representation by Tensors and Matrices*, Clarendon Press, Oxford.

48. Altair. 2016, *HyperWorks 14.0 Desktop User Guides*, http://www.altairhyperworks.ca/.

49. Abdelhamid, M., and Czekanski, A. 2016, "On the effective properties of 3D metamaterials", *ASME, Volume 9: Mechanics of Solids, Structures and Fluids; NDE, Diagnosis, and Prognosis*, ASME, Phoenix, USA.pp. V009T12A062.

50. Formlabs. 2017, *Online Documentation*, https://formlabs.com/.

51. ASTM. 2014, "D638 Standard Test Method for Tensile Properties of Plastics", *Annu B ASTM Stand*,pp. 1-15.

52. Stratasys. 2017, *Online Documentation*, http://www.stratasys.com/.